ORNL/TM-2021/2160

Artificial Intelligence for Multiphysics Nuclear Design Optimization with Additive Manufacturing

B. D. Hiscox
E. L. Popov
R. K. Archibald
V. Sobes
B. J. Ade
N. D. See
B. R. Betzler

August 2021

M2TC-21OR0404032

OAK RIDGE National Laboratory

ORNL/TM-2021/2160

Transformational Challenge Reactor Program

ARTIFICIAL INTELLIGENCE FOR MULTIPHYSICS NUCLEAR DESIGN OPTIMIZATION WITH ADDITIVE MANUFACTURING

B. D. Hiscox [a]
E. L. Popov [a]
R. K. Archibald [a]
V. Sobes [b]
B. J. Ade [a]
N. D. See [a]
B. R. Betzler [a]

[a] Oak Ridge National Laboratory
[b] University of Tennessee, Knoxville

August 2021

M2TC-21OR0404032

Prepared by
OAK RIDGE NATIONAL LABORATORY
Oak Ridge, TN 37831-6283
managed by
UT-BATTELLE, LLC
for the
US DEPARTMENT OF ENERGY
under contract DE-AC05-00OR22725

CONTENTS

LIST OF FIGURES

LIST OF TABLES

ABBREVIATIONS

AI	artificial intelligence
AM	additive manufacturing
BWR	boiling water reactor
CFD	computational fluid dynamics
GP	Gaussian process
HPC	high-performance computing
MCNP	Monte Carlo N-Particle
ML	machine learning
ORNL	Oak Ridge National Laboratory
PWR	pressurized water reactor
R&D	research and development
TCR	Transformational Challenge Reactor
TRISO	tristructural isotropic

EXECUTIVE SUMMARY

The geometric flexibility of additively manufactured metals and ceramics generates a very large and open design space that requires advanced modeling and simulation tools for physics simulations and the rigorous definition of design problems. This effort deploys artificial intelligence (AI) and machine learning (ML) algorithms to understand the design space, evaluate potential designs, and more efficiently generate optimized results.

The Transformational Challenge Reactor (TCR) program is leveraging advances in several scientific areas—including materials, manufacturing, sensors and control systems, data analytics, and high-fidelity modeling and simulation—to accelerate the design, manufacturing, qualification, and deployment of advanced nuclear energy systems. Through a manufacturing-informed design approach, the TCR program seeks to integrate digital data for rapid nuclear innovation; accelerate the adoption of advances in manufacturing, materials, and computational sciences for nuclear applications; and dramatically reduce deployment costs and timelines for new nuclear reactor technologies.

This report documents efforts under the TCR program to leverage advanced modeling and simulation techniques driven by AI/ML algorithms on high-performance computing (HPC) systems to yield more optimized TCR core designs. A multiphysics ML surrogate model was developed to run on the HPC architectures. The surrogate model is trained on high-fidelity simulation data of coupled neutronics and thermofluidics and is used to quickly evaluate thousands of candidate core designs in parallel, which drives the evolution of the cooling channel shapes to minimize temperature peaking and material stress. Outcomes from these activities provide design information and feedback into the core design efforts.

1. INTRODUCTION

Continued developments in advanced manufacturing technologies are fundamentally altering how components are designed and manufactured [1, 2]. The potential application space for these technologies within the nuclear industry is very broad because of the rigorous requirements and inherent multidisciplinary nature—encompassing civil, mechanical, electrical, and nuclear engineering—of large nuclear power plants [3]. Beyond applications for existing nuclear reactors, these new manufacturing methods, advanced materials, and dimensional constraints can be applied to the nuclear core design problem [4, 5]. A manufacturing-informed design approach yields the most benefit from the application of advanced manufacturing in the nuclear industry [6-9], leveraging advanced materials, data science, and rapid testing and deployment to decrease costs and development times and ultimately improving future commercial viability. This approach is being demonstrated under the US Department of Energy Office of Nuclear Energy's Transformational Challenge Reactor (TCR) program [10].

The availability of advanced manufacturing technologies to realize complex nuclear structures presents a core design challenge [4, 5] beyond simple applications to replace noncritical reactor components [11]. The freedom in geometric complexity offered by advanced manufacturing presents a challenging multiphysics analysis and optimization problem. A successful core design would exploit the advantages offered by advanced manufacturing and demonstrating this reactor core would showcase these benefits in a tangible manner, greatly advancing the understanding of advanced manufactured component performance in these harsh environments.

1.1 ARTIFICIAL INTELLIGENCE FOR NUCLEAR ENGINEERING

Artificial intelligence and machine learning have gained significant use in numerous topics in nuclear engineering. A summary of the current status of using AI/ML for existing nuclear power plants related to nuclear reactor heath, monitoring, and radiation detection is provided by Gomez-Fernandex et al [12]. AI techniques are also being applied to numerous nuclear data problems including nuclear data uncertainty [13], identification of problems in nuclear data [14, 15], and aiding in performing nuclear data evaluations [16-18]. AI/ML techniques have also gain popularity for nuclear material security applications, the current status of which is summarized by Alamaniotis and Heifetz [19].

In the reactor design space, AI/ML techniques were initially applied to pressurized water reactor (PWR) and boiling water reactor (BWR) core reload optimization [20-23]. Core reload design and analysis is an especially attractive area for use of AI/ML optimization techniques for numerous reasons: (1) there is significant economic benefit to fuel vendors and operators of existing plants if more power can be produced from a particular core design, (2) the primary modeling and simulation tools for these systems are well established and run quickly to support many core design iterations, (3) the problem has sufficient constraints to make AI/ML techniques feasible on reasonable sized computing systems, and (4) the objective functions are well defined (excess reactivity, power peaking, etc.). Frequently, AI/ML techniques for reactor design require many simulations.

More recently, these techniques have been applied to other reactor types including high temperature gas cooled reactors [24-27], molten salt reactors [28], and research reactors [29-32]. A more complete summary of the open-ended nuclear design R&D that predates and motivated this work are provided in Section 2.1.

1.2 ADDITIVE MANUFACTURING FOR NUCLEAR ENGINEERING

The technology readiness of many additive manufacturing (AM) processes has greatly increased in recent years. Plastic and polymer AM has become ubiquitous; however, these materials are not applicable for

most nuclear engineering applications. Metal and ceramic AM processes offer far greater promise for nuclear systems and are being pursued by government-funded research institutions, universities, and industry.

Interest in AM for nuclear applications typically falls into one of four basic areas:

- prototyping;
- manufacturing jigs, fixtures, special tooling, and so on to aid in a traditional manufacturing process;
- replacing components that are obsolete, difficult to manufacture, costly, or have long lead times in existing reactors; and
- constructing components for new reactors.

The TCR program has leveraged the ability to rapidly produce components to accelerate the design of nuclear systems. The ability to physically interact with a component and assemble multiple components leads to deeper and faster learning than the typical nuclear design processes. The TCR program is currently constructing a full-core demonstration core that will improve understanding in several areas, including: (1) deviating additively manufactured components from the as-designed component, (2) fitting additively manufactured components to traditionally manufactured components, (3) welding additively and traditionally manufactured components to one another, and (4) assessing the tolerance stack-up when assembling many additively and traditionally manufactured components.

For existing reactors, replacing components that are obsolete or difficult to manufacture offers a gateway into using AM components in irradiation environments. Through a partnership with Framatome and the Tennessee Valley Authority, the TCR program produced and additively manufactured a safety-significant fuel assembly bracket (Figure 1) that is produced via conventional means. This fuel assembly bracket is currently used in the Browns Ferry reactor as a real-world application for nuclear components in a reactor.

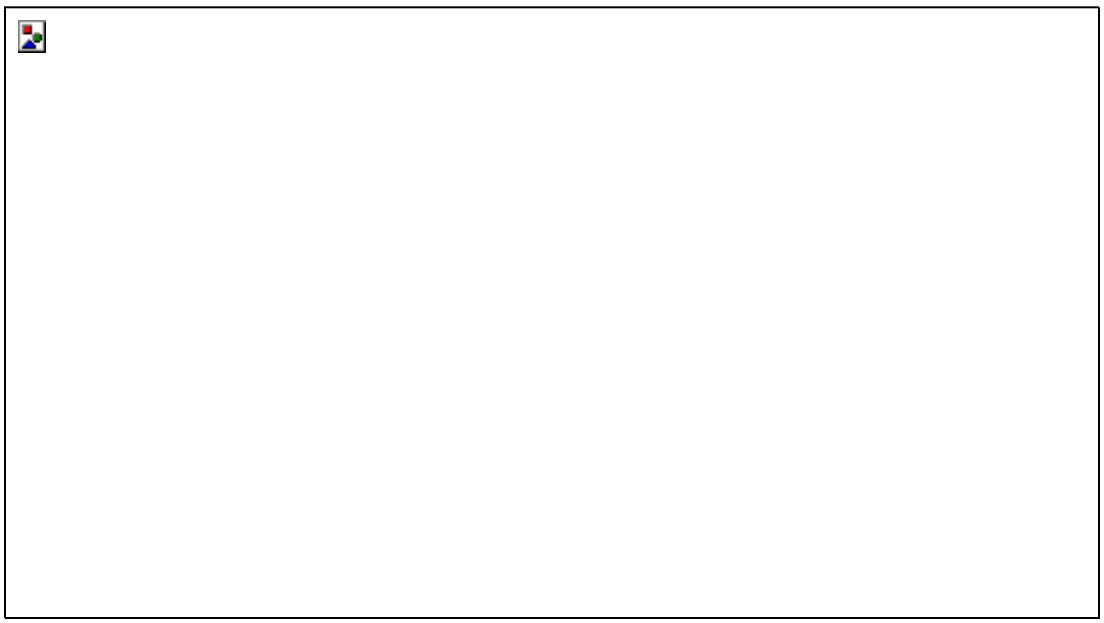

Figure 1. 3D printed fuel assembly brackets produced by ORNL for Framatome and Tennessee Valley Authority.

Additionally, Westinghouse Electric Company used AM to produce a thimble plugging device that is currently used in Exelon's Byron Unit 1 (Figure 2). This component is used to help lower fuel assemblies into the reactor [33].

Figure 2. Westinghouse Electric Company 3D printed thimble plugging device.

Although these accomplishments show positive progress toward the use of AM in nuclear reactors, a far greater yet achievable milestone would be deploying an advanced reactor design whose performance is improved through AM features. AM of nuclear fuel-related structures has been an R&D topic in both the TCR program [34] and elsewhere [35-38]. Some approaches could significantly increase nuclear core performance; however, these newer technologies are likely still years away before they could be adopted for a demonstration reactor. Alternatively, most of the work performed under the TCR program focused on developing a process to combine an additive and a traditional fuel manufacturing process. The TCR fuel form consists of conventionally manufactured UN tristructural isotropic (TRISO) fuel particles embedded inside a 3D printed SiC matrix [6, 39, 40]. In the TCR fuel form, TRISO particles are poured into a 3D printed SiC shell, creating a fuel form that has all the features one might expect from a fully additively manufactured fuel element (e.g., complex surface features, complex cooling channels, variable fuel density), as shown in Figure 3, but constitutes a more near-term deployable fuel production process.

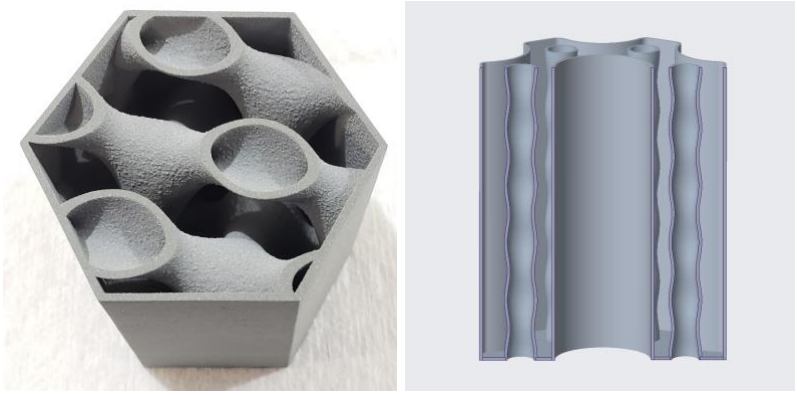

(a) (b)

Figure 3. (a) Printed SiC element showing the complexity possible using AM), and (b) coolant channel surface features postulated for thermal performance improvements.

Within the processes developed under the TCR program, each fuel element could contain different fuel loading, different cooling channel design, different surface features, and so on. This flexibility is afforded through the additive process, which does not require different molds, dies, or other tooling to produce

varying fuel elements designs. Even within the constraints of the TCR design, there is a large design space that can be fully evaluated only via advanced means. With its dimensional control and ability to print features impossible through traditional processes, AM is well suited to deliver the potential gains postulated by advanced design optimization using artificial intelligence (AI) and machine learning (ML) processes.

1.3 PURPOSE AND SCOPE

Several efforts under the TCR program have been related to design optimization; however, many of these use traditional optimization approaches apply to a portion of the reactor system (Appendix A). Open-ended design optimization was pursued by Sobes et al. [41] in previous work. Sobes et al. focused on optimizing a basic fuel shape in a flow field. The results indicated that a nonintuitive shape, a truncated annular cone, was best when given the chosen optimization parameters.

The goal of the current effort was to leverage the previously developed tools but for a more constrained geometry with the results applied to real-world work ongoing under the TCR program. That is, the overall flexibility in the geometry must be constrained around a cylindrical central moderator rod with a stainless-steel tube because this is the currently preferred method for encapsulating YH_x. However, internal hole in the YH_x (e.g., the channel shape and size) is allowed to vary throughout the core. By allowing these variables to change, the neutronic and thermofluidic performance can be optimized together.

The preliminary TCR design was used as a starting point. By using the traditionally designed TCR core as a basis, the results can be directly applied to yield a more optimized core design that can achieve higher performance metrics than traditional design. The full-core design optimization is large and requires new modeling and simulation approaches and tools. The development of these tools and their deployment on high-performance computing (HPC) systems for TCR design optimization are presented herein.

2. NUCELAR DESIGN OPTIMIZATION

The specific need for AI application to the nuclear design problem stems from the vast design space enabled by advanced manufacturing and the demonstrated sensitivity of nuclear system performance to small changes in the geometric design. Advanced manufacturing allows precise and detailed changes to be made in the geometry of a nuclear system, such as the TCR demonstration core, which can significantly improve reactor performance. However, the space of the possible changes in the geometric design is so large that it reaches beyond the grasp of human designers to see and realize all opportunities. Therefore, ML algorithms are necessary for learning all the detailed dependencies of the design performance on the geometric configuration. Furthermore, AI optimization algorithms are then needed to fruitfully use the captured knowledge of these dependencies to purposefully improve the nuclear system design.

2.1 APPLICATIONS

Two early demonstrations of the application of AI-based nuclear systems optimization are given in this section as motivation for the main work.

The first demonstration of the coupling of advanced manufacturing and AI-based optimization is in the design of axial fuel loading. Uniform fuel loading in the axial direction results roughly in a cosine power distribution, but a flat power distribution is desirable for many engineering reasons. In traditional light water reactor designs, the tendency for the cosine power distribution is counteracted by a combination of variable fuel and fixed-burnable-poison loading in the axial direction, control rod position, and axial coolant density variation. In an example optimization exercise, the cosine power distribution was counteracted by a variable fuel density in the axial direction [42]. The results show that a significant reduction in the axial power peaking is achievable by varying the density of the fuel and moderator in the axial direction during a manufacturing process, as shown in Figure 4.

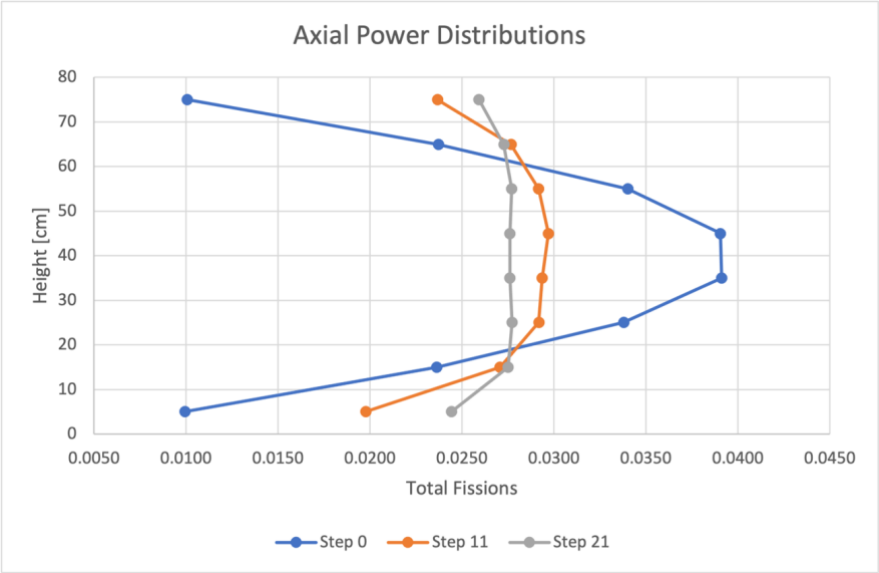

Figure 4. Achieved axial power flattening by changing the density in axial fuel zones [42].

This simple demonstration shows the ability of advanced manufacturing techniques to solve engineering problems by simpler means (i.e., there is no need for axially variable burnable poison loading).

Furthermore, in this demonstration, the optimal solution is intuitive to the nuclear engineer, allowing the AI optimization to be easily interpreted and verified.

The second demonstration example is the optimization of the cooling channel designs for a cylindrical reactor [43, 44]. The basis of this demonstration problem was to determine the optimal geometric shape in the axial dimension of the cooling channels of a simplified nuclear reactor design's full-core model. The core is a right cylinder that is 1 m in diameter and 80 cm tall. Nine concentric rings of hexagonal assemblies surround a central hexagonal assembly. The fuel is annular with a 2.5 cm outer diameter, and it sits in the middle of each 5 cm wide (flat to flat) hexagonal assembly. There are cooling channels inside the annular fuel, and the moderator surrounds the outside of the fuel annulus. The center assembly in the core is a pure moderator, uncooled and unfueled. The coolant flows from the bottom to the top in all the fueled assemblies. Figure 5 presents a core schematic. This design is different from the current TCR design because the structure of the fuel and moderator are reversed. However, the optimal design of the axial evolution of a cooling channel is very informative and generalizable.

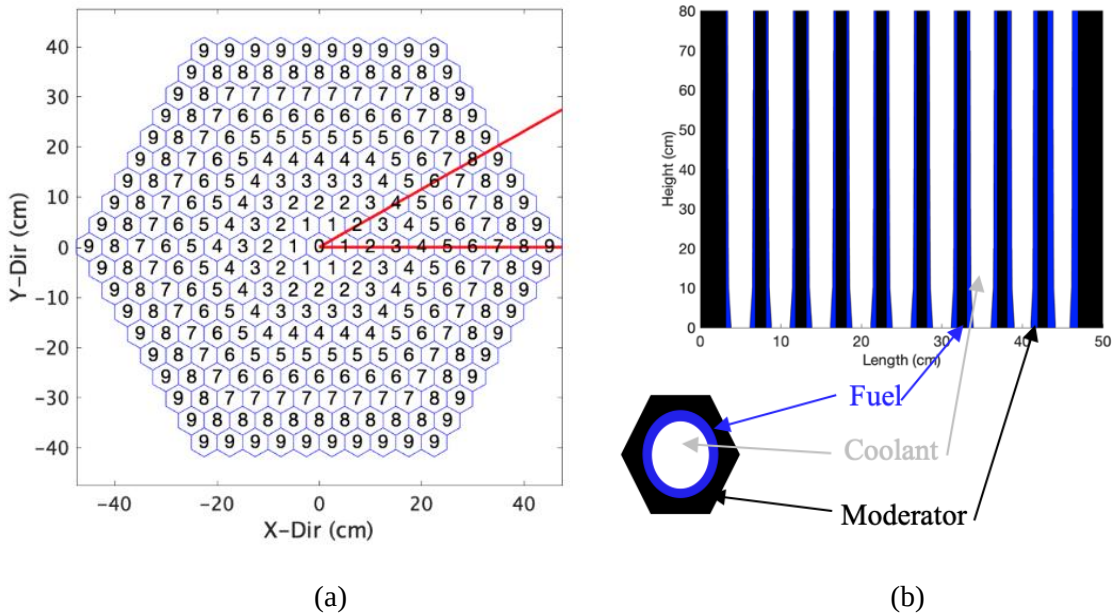

(a) (b)

Figure 5. (a) Top view of the core with the nine radial assembly rings labeled. Only the symmetric 1/12 segment inside the red lines is modeled. (b) A horizontal slice of one assembly and an axial cross section of the optimized core configuration.

The design space encompassed the coolant channel axial profile in each of the nine assembly radial rings. That is, all the assemblies in each ring had the same coolant channel axial profile, but the profile was different for each radial assembly ring. The objective for this core design was to minimize the temperature peaking factor across each 10 cm vertical segment (eight making the full axial height) of each assembly while maintaining a critical core configuration. The engineering justification for this objective function was to minimize the mechanical stresses due to temperature gradients in the components, although no thermomechanical analyses were performed in this initial study. Specifically, the objective function is defined as:

$$F(\Phi) = \frac{1}{10}\sum_{i=1}^{10} \quad \{max\, T(x,y,z,\Phi) - min\, T(x,y,z,\Phi): 8(i-1)\, cm \le z \le 8i\, cm, (x,y,z) \in Fuel\}, \tag{1}$$

where $T(x, y, z, \Phi)$ is the temperature at the location (x, y, z) and design parameters Φ.

This problem inherently requires multiphysics modeling between neutron transport and thermofluidics. The problem is further convoluted because the cooling channel radius (axially variable) simultaneously controls everything about the heat transfer process and the amount of fuel at each axial core level because the fuel annulus outer diameter is fixed. The predictive simulation of candidate configurations requires computationally intensive modeling. The authors used a Monte Carlo-based code for neutron transport coupled to a computational fluid dynamics (CFD) code for the thermofluidics. With a large potential design space to explore, it was impractical to evaluate all the candidate designs with the full-fidelity physics. Therefore, the authors developed an ML-based multiphysics emulator that was designed to run on the Summit supercomputer, a GPU-based HPC system [45], at Oak Ridge National Laboratory (ORNL). By training the ML-based emulator, the authors achieved errors as low as a few percent, which allowed them to quickly and reliably sample thousands of candidate designs on Summit. Only the most promising candidate designs were tested with the full-fidelity physics simulations. The emulator was updated, and convergence on the optimal design was achieved in only a few iterations.

The quantitative objective function for the challenge problem's optimization design was to minimize temperature peaking in each 10 cm axial section (eight total for the full-core height) of each assembly in the core. From single-assembly simulations, the average numerical value of the objective function for a conventional design with axially uniform coolant channels of one radius was 842.1°C. The optimal design results in a final value of the objective function of 291.35°C. A 3-fold improvement in the objective function is achieved through the AI-based optimization of the geometry of the cooling channels when compared with the constant-cooling-channel-radius design. Figure 6 presents the visualization of the calculated temperature distribution in the core before and after the optimization.

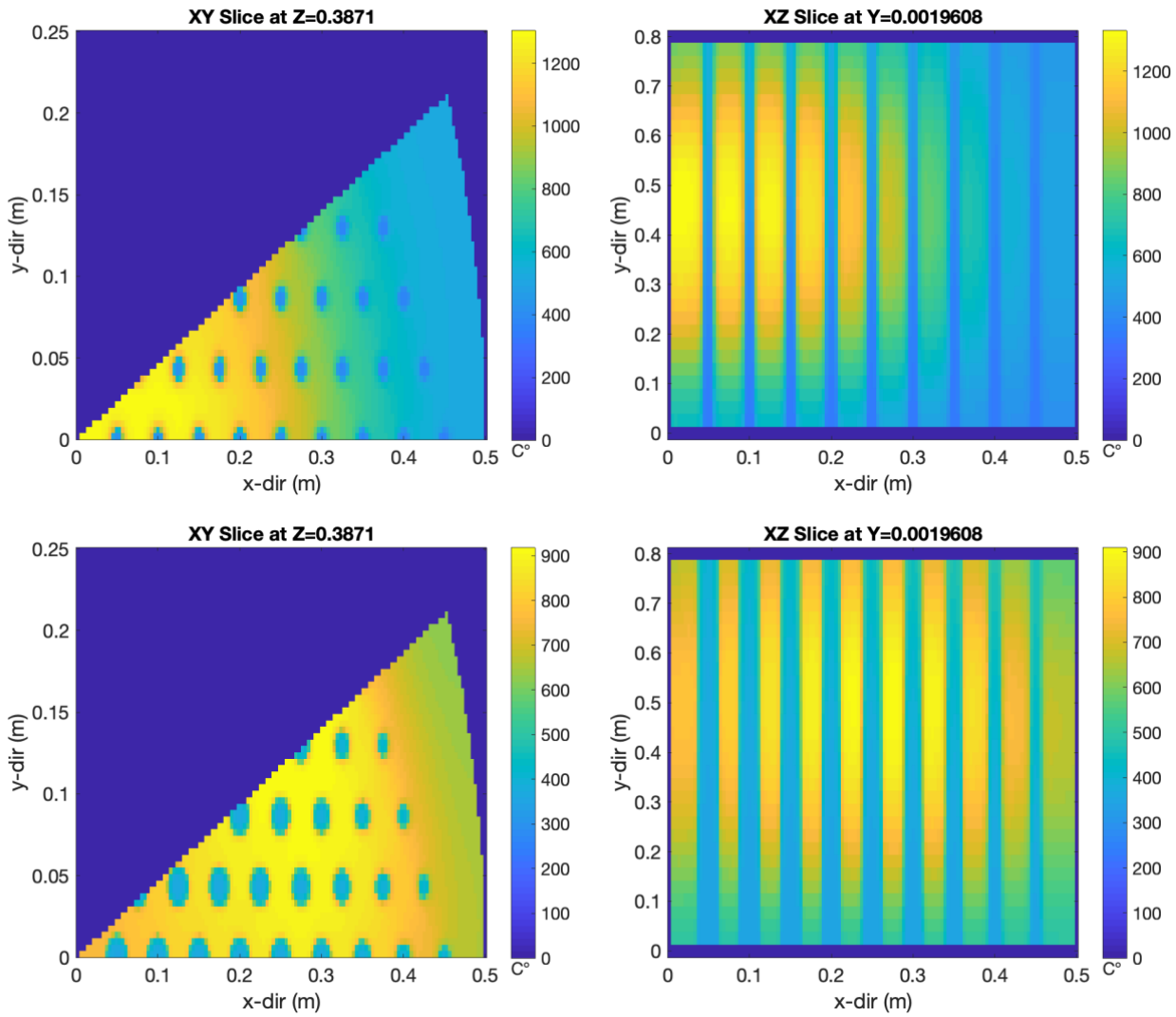

Figure 6. Visual representation of the temperature distribution in the original (top) and optimized (bottom) cores. The two left-most figures present a radial slice at an axial location of 38.7 cm out of a total core height of 80 cm. The two right-most figures present an axial slice through the core.

Figure 7 presents a physical interpretation of the optimization results by plotting the fuel volume in each assembly and the heat-exchange area for the cooling channels. The initial configuration with axially uniform cooling channels in all assemblies is shown in black. This presents the optimal solution for a uniform cooling channel configuration. An intermediate stage of the optimization process is shown in blue, and the final, optimal design is shown in green. The intermediate result can be identified by the rough behavior of the volume and surface plots across the nine radial assembly rings, whereas the converged solution displays the physically expected smooth behavior. Furthermore, there is a trade-off between the increased heat-exchange area of the cooling channel and the reduced fuel volume. Both contribute in the same direction to reducing the temperature peaking in the middle of the core that is observed with the uniform cooling channel design.

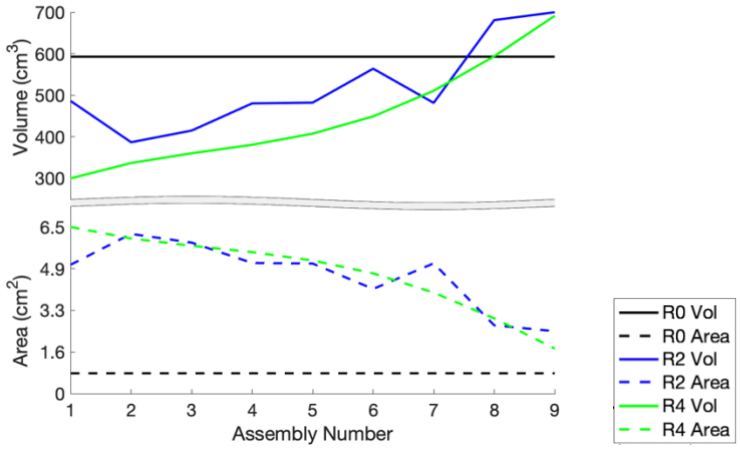

Figure 7. Plot of the fuel volume per assembly (top) and the heat-exchange area for the cooling channel in each assembly (bottom). The three different colors represent different iterations of the optimization algorithm: the initial iteration (R0) and two later iterations (R2 and R4). *R0*, *R2*, and *R4* are shorthand for iteration round zero, two, and four, respectively.

Although the optimal configuration can be justified from an engineering analysis perspective, the result is far from trivial. The right-hand side of Figure 5, which plots the axial cross section of the optimal design, shows that the profile of the cooling channels changes in two dimensions: axially with the height of the core and radially across the different assembly rings. The cooling channel shape is also unique for each radial assembly ring rather than being a scaled or translated version of each other. The top plot in Figure 7 also shows a significant reduction in the fuel volume needed to maintain the reactor as critical at a fixed power level compared with the traditional, uniform design. Lastly, the extension of this result is that the reactor can be operated at higher power levels for the same amount of fuel and peak fuel temperature limits.

2.2 MODELING AND SIMULATION

2.2.1 Optimization Work Flow: Inner and Outer Loops

The authors identified two categories of tasks necessary for successfully developing a holistic AI-based approach to computationally optimizing nuclear systems. The tasks are separated into the inner computational loop and the outer optimization loop. The inner computational loop involves the full-fidelity physics simulation of the candidate designs needed to create the training data for the multiphysics ML-based emulator. The outer optimization loop begins with training the emulator based on the results generated with the full-fidelity physics calculations, and design parameters are chosen from a random sample of the design space. The outer optimization loop is the AI model for the design space that is updated based on massively parallel evaluations of the multiphysics emulator on thousands of candidate geometries. Figure 8 illustrates the workflow. The outer loop can be thought of as an adaptive sampling method ubiquitous in computation design [46] in which each iteration focuses on a smaller design space that minimizes the given loss function.

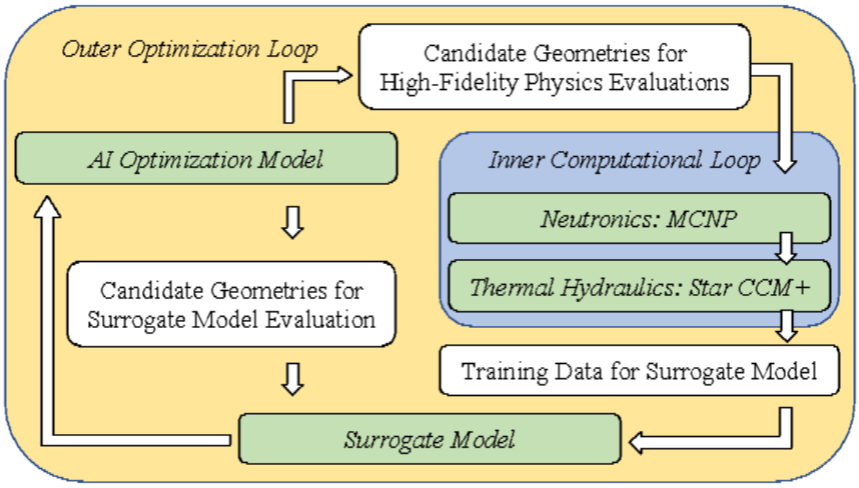

Figure 8. Illustration of the AI optimization workflow.

2.2.2 Inner Computational Loop

The neutronic modeling for this project was conducted in the Monte Carlo N-Particle (MCNP) code [47, 48]. This code was chosen because of its ability to calculate power in nonfuel materials. This allowed for a very accurate power density profile in all materials. To save on computational time, the model was 30°of the full core (1/12) with reflective boundary conditions (i.e., instead of the full 360°). Because of the intrinsic symmetry and core optimization variables, this model represents a full-core model. The model was run with four tally meshes to account for the energy deposition in a cell from neutrons and photons in the fuel and moderator materials. A tally was produced for each mesh bin. The mesh bin density was 504 in the *x* direction, 252 in the *y* direction, and 20 in the *z* direction. Therefore, the lengths of each mesh bin were 0.1, 0.1, and 4 cm. These sizes were determined because they have a reasonable computational cost neutronically and thermofluidically, and meshing studies determined that they were sufficiently fine to achieve good resolution on the fuel annulus and coolant channels. The power density was normalized to maintain a constant core power.

There were 750 cycles run with 10,000 particles in each cycle. The first 50 cycles were inactive, which means they were not taken into account for the determination of k_{eff}, flux, or reaction rates. There must be inactive cycles in the beginning for the sake of convergence. The average standard deviation in k_{eff} was 0.00024, and the maximum was 0.0003. The power density was normalized to maintain a constant core power. MCNP was run in "mode N P," which accounts for neutron-induced photons. This is necessary for the photon tallies.

The thermofluidics model developed for this work relies on numerical methods (e.g., temporal and spatial discretization) and physical models (e.g., turbulent flow, conjugate heat transfer) to predict the temperature and flow distribution in the geometry of interest. The inherent assumptions of these methods and models must be quantified to ensure the correctness and accuracy of the results. In view of the diverse geometry configurations of the optimized designs, an accurate prediction of temperature distribution in the component is necessary. The thermofluidic model must be capable of computing a conjugate (i.e., solid fluid) heat transfer in arbitrary geometric shapes. To achieve this, a CFD approach was taken, and the commercial software STAR-CCM+ was used [49]. This method allows complex surfaces to be discretized with finite volume techniques and allows the interface between the solid structure and the coolant—gas, in this case—to be properly defined. On the solid side, a thermal diffusion of heat with a volumetric heat source is computed to determine the temperature distribution. The heat generated by

nuclear fission is deposited in the core element according to the volumetric power distribution supplied by the reactor physics calculation.

On the fluid side, a Reynolds averaging of the velocity vector field was employed within the finite volume formulation. Because the assumed flow is highly turbulent, a two-equation model of turbulence, realizable k-epsilon, was used. This model is better than the standard k-epsilon model for many applications, including rotational and shear flows, and it generally gives answers that are at least as accurate [50]. The near-wall velocity field is resolved with the two-layer all wye (Y+) plus method [49]. All these models accurately predict the wall heat transfer, which is critical for the proper resolution of the component temperature field.

A geometry parameterization method was used to model the geometry variation necessary for running the suite of optimization codes. Within the CFD computation, the geometry is regenerated automatically every time a new combination of parameters is tried. The software allows the computational domain to be modified in both its geometry and discretization without user intervention. This is achieved by automating the computing process with Java drivers. The approach is fully integrable in an autonomous workflow within the entire optimization suite.

For the thermofluidic calculation, the domain was discretized with a variable resolution but with at least four elements in the radial direction across fuel. A polyhedral mesh with a base dimension determined by the smallest fuel element was used. Because the geometry varies by fuel and channel sizes, the number of elements per case is different and usually stays below 7 million. Some specific cases with thin fuel might increase the element count to 20 million, but this is rare. The calculations were run in parallel on 16 processes, and most run time was spent on grid generation. The average clock time for a single run is around 2 h. The cases were run until the convergence of momentum and energy residuals for at least three orders of magnitude was achieved. Sensitivity on mesh and residuals convergence was performed to allow for temperature accuracy of less than 1° to be achieved. The employed modeling approach relies on component physics validation, which is part of the software qualification process implemented at ORNL. The flow and heat transfer solutions, as well as the corresponding modeling techniques, were initially tested and verified by standard test problems. The models will be further tested against integral experiments after some are performed as part of a comprehensive testing program.

Figure 9 illustrates a typical result from the thermofluidic solution. Contours of temperatures are shown at three axial levels in the core: lower (15 cm), middle (45 cm), and upper (75 cm). The highest temperature is reached in the exit core plane. Radial variation of cooling channels, fuel, and moderators is defined by the optimization algorithm. Channels are larger in the central part and smaller at the periphery where the power density is lower and less coolant is needed. The average pressure drop, fuel temperature, and maximum fuel temperature difference were also calculated and are provided for reference. The input power density is plotted on the left-hand side of Figure 9 at the same axial positions. The simulation used power deposition in the fuel and moderator. The results shown are from a random set of input parameters. They do not represent an optimal configuration but are provided for reference as typical data transferred from the high-fidelity (physics simulator) solution to the ML emulator.

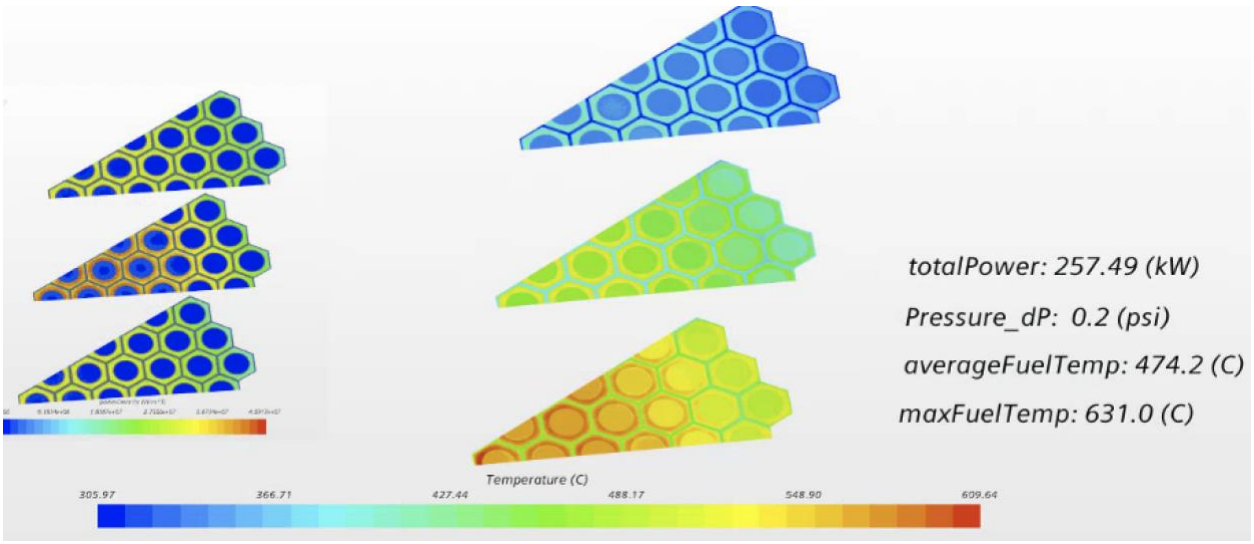

Figure 9. Temperature field from the thermofluidic solution. Three axial sections are plotted at lower, middle, and upper core element levels. They show the temperatures in the coolant, fuel, and moderator. The power input to the fuel and moderator is shown on the left.

2.2.3 Outer Optimization Loop

Simulation-based computational design can quickly become an intractable problem, depending on the size of the computational design space and computational complexity of the design simulation. The authors developed reduced-order surrogate models for neutronics and thermofluidics that can quickly sample hundreds of thousands of geometries on Summit. By using the combination of surrogate modeling and sparse validation with correction from full-physics simulations, the authors were able to train Gaussian process (GP) ML methods to accurately predict optimal designs. On average, one reactor core design takes ~150 s for the reduced-order surrogate model to simulate on one Summit GPU. This time includes all setup costs and data movement. With six GPUs per node, the authors were able to test ~150 reactor geometries per hour per node. Generally, the surrogate is around 95% accurate compared with full-physics simulations that use relative least square error measurements on the objective function for this problem. Also, the surrogate model generally struggles most at the inlet region. For the core challenge problem, Summit simulated ~10,000 different geometries in combination with ~100 full-physics simulations in four iterations to determine an optimal design.

The outer loop AI model is based on the GP, which is a kernel-based ML method that provides an efficient method for ML applicable to physics-oriented problems in engineering sciences. Specifically, given a set of training data:

$$\{(p_i, P_i(x), T_i(x), V_{i,c}(x), V_{i,f}(x), V_{i,m}(x), L_i, \sigma_i) : i = 1, \ldots, N\}, \quad (2)$$

the loss can be determined for any parameter set. Here, x is the position vector, and p_i is the parameter vector for the i^{th} design. The functions are the power P_i, component temperature T_i, fractional coolant indicator $V_{i,c}$, fractional fuel indicator $V_{i,f}$, and fractional moderator indicator $V_{i,m}$ for N simulated training sets. The loss L_i for any design is defined as the standard deviation of temperature for every domain with a positive fuel indicator. The last item in this collection is the error estimation of the loss σ_i. The loss of any design p is predicted by using the kernel-based ML method defined as:

$$L(p) = \sum_{i=1}^{N} \quad c_i k(p, p_i), \quad (3)$$

where kernel function $k(p,p_i) = e^{-\frac{1}{2}\|p-p_i\|^2}$ is used. The coefficients of the kernel-based ML are found by solving:

$$L_j = \sum_{i=1}^{N} \quad c_i k(p_j,p_i) \equiv Kc, \tag{4}$$

for $j = 1,\ldots,N$ training sets, where L_j losses are known. The matrix elements are given as $K_{i,j} = k(p_i,p_j)$ for $1 \le i,j \le N$ and the coefficient vector $c = (c_1,\ldots,c_N)$.

The data from the full-fidelity physic model are augmented with a set of *M* emulated models:

$$\{(p_i, P_i(x), \tilde{T}_i(x), V_{i,c}(x), V_{i,f}(x), V_{i,m}(x), L_i, \sigma_i) : i = N+1,\ldots,N+M\}. \tag{5}$$

The ML method assumes that the full-fidelity physical models are exact, or $\sigma_i = 0$ for $i = 1,\ldots,N$. In the case of $i = N+1,\ldots,N+M$, a low-resolution approximation of the physics is used to estimate the temperature function $\tilde{T}$ by solving:

$$-\left(\alpha_c V_{i,c}(x) + \alpha_f V_{i,f}(x) + \alpha_m V_{i,m}(x)\right)\Delta\tilde{T}_i(x) = v_i(x)\frac{\partial \tilde{T}_i(x)}{\partial x} + P_i(x), \tag{6}$$

where $v_i(x)$ is a flow field, $\frac{\partial \tilde{T}_i(x)}{\partial x}$ is the temperature gradient along the flow direction, and α_c, α_f, and α_m are constants. For any design p, the flow field is calculated based on the volumetric rate of coolant. The flow field is zero in the solid material of the reactor. The flow field and constants α_c, α_f, and α_m are calculated so that $\sum_{i=1}^{N} \quad \|T_i(x) - \tilde{T}_i(x)\|_2$ is minimized, where $T_i(x)$ is the training set temperatures.

When the data are augmented, the GP is calculated by:

$$L(p) = \sum_{i=1}^{N+M} \quad c_i k(p,p_i)\,, \tag{7}$$

where the kernel function $k(p,p_i) = e^{-\frac{1}{2}\|p-p_i\|^2}$ is used. The coefficients of the kernel-based ML are found by solving:

$$L_j = \sum_{i=1}^{N+M} \quad c_i\left(k(p_j,p_i) + \sigma_i^2\delta_{i,j}\right) \equiv Kc, \tag{8}$$

for $j = 1,\ldots,N+M$ and $\sigma_i = 0$ for $i \le N$, where the matrix elements are given as $K_{i,j} = k(p_i,p_j)$ for $1 \le i,j \le N+M$, the coefficient vector $c = (c_1,\ldots,c_{N+M})$, and σ_i is an estimate for the error in the emulation.

2.3 PROBLEM DEFINITION

The grand challenge problem for AI optimization in this work was to optimize the current TCR core design. The objective for the AI optimization was to minimize the variation (i.e., variance) of the predicted temperature distribution in each additively manufactured component of the core, as shown in Figure 10. The variance of the temperature distribution in a component was chosen as a proxy for thermal-induced mechanical stress. This assumption was verified by comparing the temperature variation in different components calculated with the thermal-fluidics STAR-CCM+ code to the thermal-induced mechanical stress calculated with the BISON fuel analysis code. More precisely, the objective was to optimize the design to minimize the temperature variation in the component with the largest stress.

The design optimization was constrained by the need for the core to be above critical and not exceed a coolant pressure drop of 4.5 psi constrained by the planned pumping power. The core power of the design was kept constant at 255 MW.

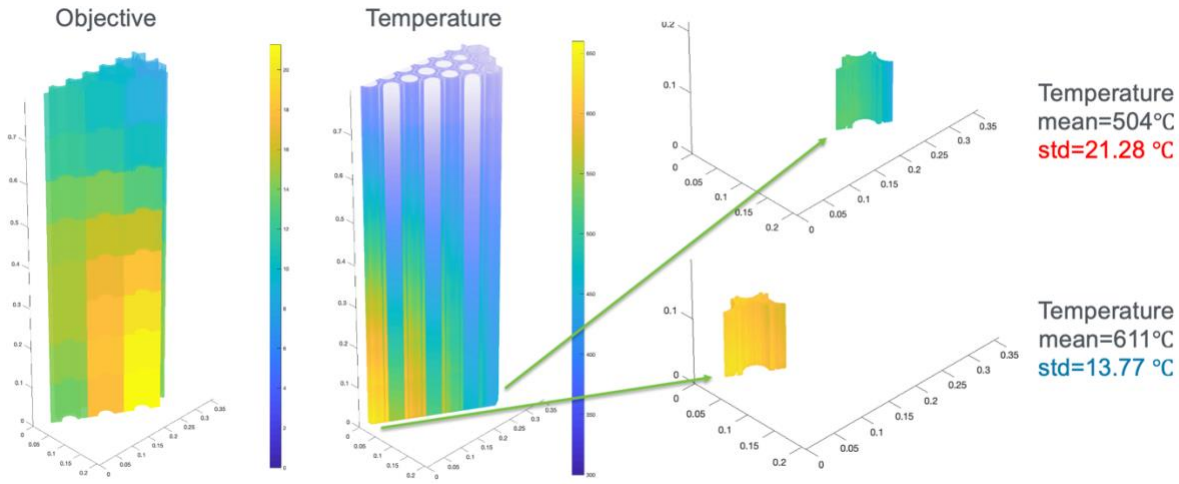

Figure 10. Visual comparison of the difference between the temperature in the core and the variation of the temperature (i.e., objective function) in each of the core elements.

3. CHALLENGE PROGRESSION PROBLEMS

3.1 OPTIMIZATION PROBLEM SETUP

To aid in the computational modeling of the inner loop, the current TCR core design was slightly modified. The top and middle plots on the right-hand side of Figure 11 demonstrate this modification. The top plot shows the original design, and the middle plot shows the modified configuration used in the optimization. Through this modification, the cog design is converted into hexagonal fuel assemblies. The objective function was always evaluated over the real core cog-shaped elements, as shown in the bottom plot on the right-hand side of Figure 11. The hexagons shown in that plot correspond to the actual TCR core baseline design fuel elements. Thus, the link between the optimization performed on an AI-suited virtual configuration and the existing design is established.

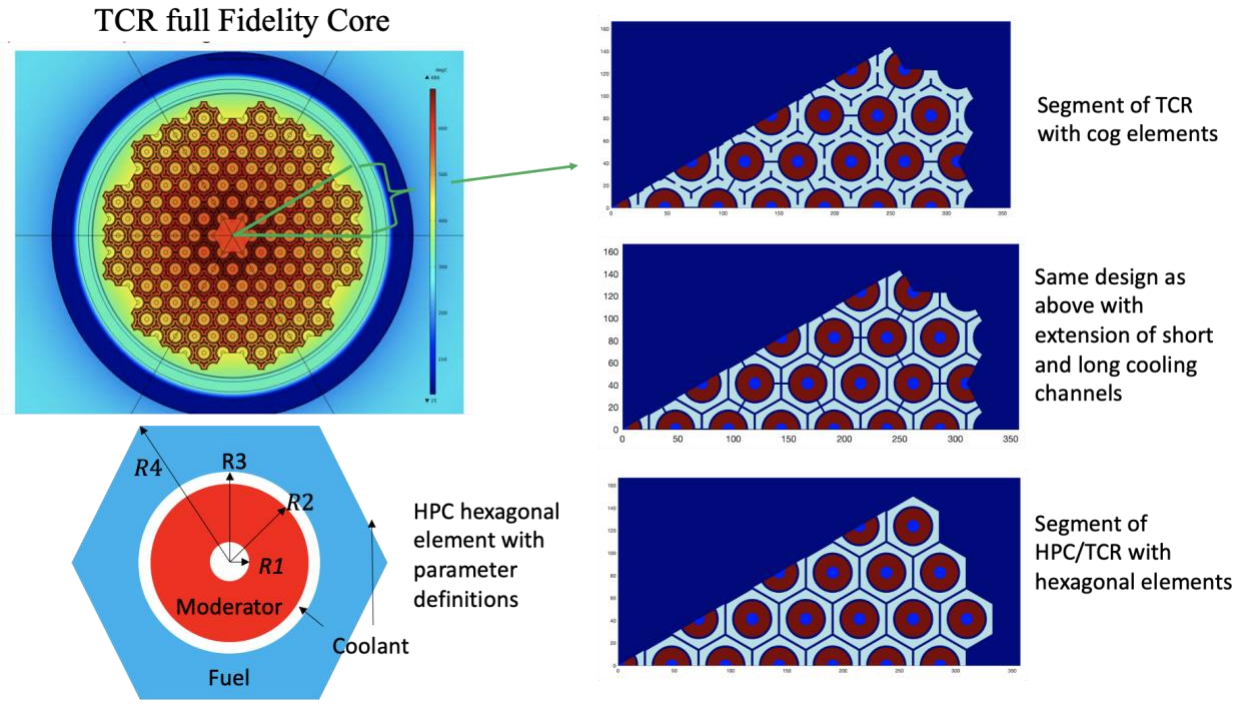

Figure 11. A full-fidelity TCR core simplified into a set of hexagonal fuel assemblies for AI-based optimization. The projected yellow hexagons in the bottom right show how the real core (cog-shaped) fuel elements overlap with the simplified hexagonal fuel elements of the optimized geometry. On the right-hand side, the coolant is shown in dark blue, the fuel is shown in light blue, and moderator is shown in red.

The simplified hexagonal-element design permits a limited number of geometry factors to be used in the optimization algorithm. Namely:

- the thickness of the moderator annulus,
- the thickness of the hexagonal fuel element annulus,
- the cooling channel gap between the moderator annulus and the hexagonal fuel element, and
- the cooling channel between neighboring hexagonal fuel elements.

The center-to-center distance of the moderator annuli was kept constant for this optimization, ensuring that the total number of fuel and moderator assemblies in the core remained fixed.

3.2 FOUR PARAMETER OPTIMIZATION OF THE BASELINE DESIGN

This step aimed to validate the optimization results and attempts to improve the baseline design. The validation step was achieved by keeping the parameters the same as in the baseline design and comparing key reactor core metrics (e.g., temperatures and mass flow rates). The four parameters were the same for all components in the core, which eliminated the radial profiling feature. This demonstrates the flexibility of the optimization-adapted model to reproduce the current (baseline) TCR design performance. Therefore, the hypothesis was that the AI-based optimization would validate that the baseline design was near-optimal.

Initially, the core parameters (four in this case), were set to match the baseline design. An optimization run was completed and key reactor factors were compared. The results are provided in Table 1. It is clearly seen that the computed temperatures for major core components (fuel elements and moderators) are almost identical. The optimization model tends to predict slightly higher maximum values which is due to the modification of cooling channels which were converted from 'wish-bone' shape to hexagonal shape as shown in Figure 11. The largest differences were observed for the coolant velocities. It was found that the values predicted by the optimization models are more accurate and led to corrections in the baseline design. This verification step confirmed the model adequacy and provided a basis for the applicability of these models in the AI algorithms.

Table 1. Verification of the optimization results for the baseline design with key core characteristics.

Reactor operational parameter	Baseline design value	Optimization model value
Coolant temperatures, ℃		
- inlet	300	300
- outlet	500	498
Fuel temperatures, ℃		
- maximum	621	654
- minimum	312	313
Moderator temperatures, ℃		
- maximum	556	564
- minimum	300	302
Coolant flows		
- max. channel velocity, m/s	46	14.6
- avg. channel velocity, m/s	26	9.9

The resulting optimum design confirmed that the baseline design was near the optimal (Figure 12). The peak temperature variance across all fuel elements (cogs) was only reduced from 14.3°C in the baseline design to 13.5°C in the optimized design. It was observed that the AI optimization:

- increased the coolant cross-sectional area to promote better cooling;
- increased the volume of the fuel with a fixed design power of 255 MW, thus effectively reduced the power density; and
- decreased the volume of the moderator, which can be seen as a compensatory result from increasing coolant cross-sectional area and increasing fuel volume while maintaining a fixed core volume.

3.3 28-PARAMETER RADIAL CORE OPTIMIZATION

In this study, the four parameters of the optimization model were allowed to vary in each of the seven radial rings bringing them to a total number of 28. This additional parameter space allowed radial profiling in the core design to minimize the temperature variation associated with the power peaking. Figure 12 depicts the core geometry of the baseline design, the optimized baseline design, and the radially optimized design. It can be seen that the hole in the YH moderator rod increased in both optimized versions of the core. The cooling channels for the radially optimized design are increased by approximately 1mm in most locations, except for the outermost radial zone.

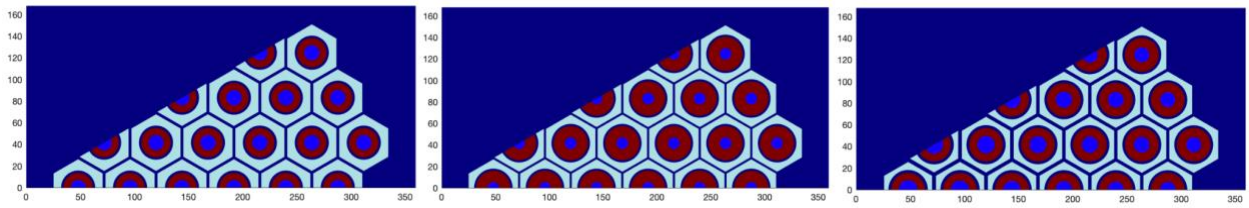

Figure 12. Variation of core geometry in the optimization process. Left - baseline design, middle - optimized baseline design, and right - radially optimized core.

Table 2 describes the differences in geometry and the core characteristics of the baseline design, the optimized baseline design, and radially optimized design. The quantities described in this table together with Figure 14 are used below to describe the changes in design parameters. The loss function drops by 26.5% from 14.7℃ to 10.8℃, while maintaining a k_{eff} above 1 and power of 255 MW. The pressure drop decreases by a factor of 2.6 (from 0.39psi to 0.15psi). The maximum temperature drops 10.7%, from 652.9℃ to 582.8℃. The reduction in the loss function and in the max temperature is visually apparent in Figure 13 that depicts the radial temperature at a slice near the exit of the core. Additionally, the radially optimized design uses less materials with a 15% decrease in total fuel and a 17.5% decrease in total moderator volume.

Table 2. Summary of parameter values and corresponding core metrics resulting from the optimization.

Parameters	Baseline Design	Optimized baseline	Radially optimized core parameter variation
R1	5.4 mm	7.0 mm	6.9-8.6 mm
R2	15.9 mm	13.5 mm	15.4-15.6 mm
R3	17.9 mm	15.7mm	17.9-18.2 mm
R4	26.6 mm	26.1 mm	25.5-26.1 mm
keff	1.1	1.0	1.0
T_{std} Cog	14.7 C	14.0 C	10.8 C
dP	0.39psi	0.26psi	0.15psi
Max T	652.9 C	659.6 C	582.8 C
Pow	255 MW	255 MW	255 MW
Fuel	$2.02\text{x}10^{-2}$ m^3	$2.42\text{x}10^{-2}$ m^3	$1.71\text{x}10^{-2}$ m^3
Mod	$1.71\text{x}10^{-2}$ m^3	$1.03\text{x}10^{-2}$ m^3	$1.41\text{x}10^{-2}$ m^3

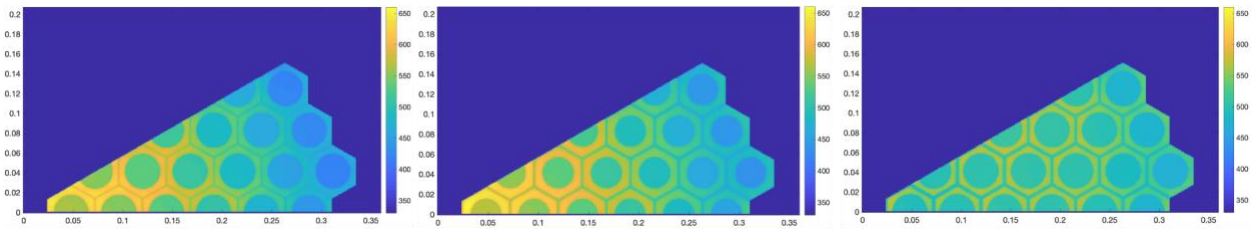

Figure 13. Variation of the objective function in the optimization process. Left - baseline design, middle - optimized baseline design, and right - radially optimized core.

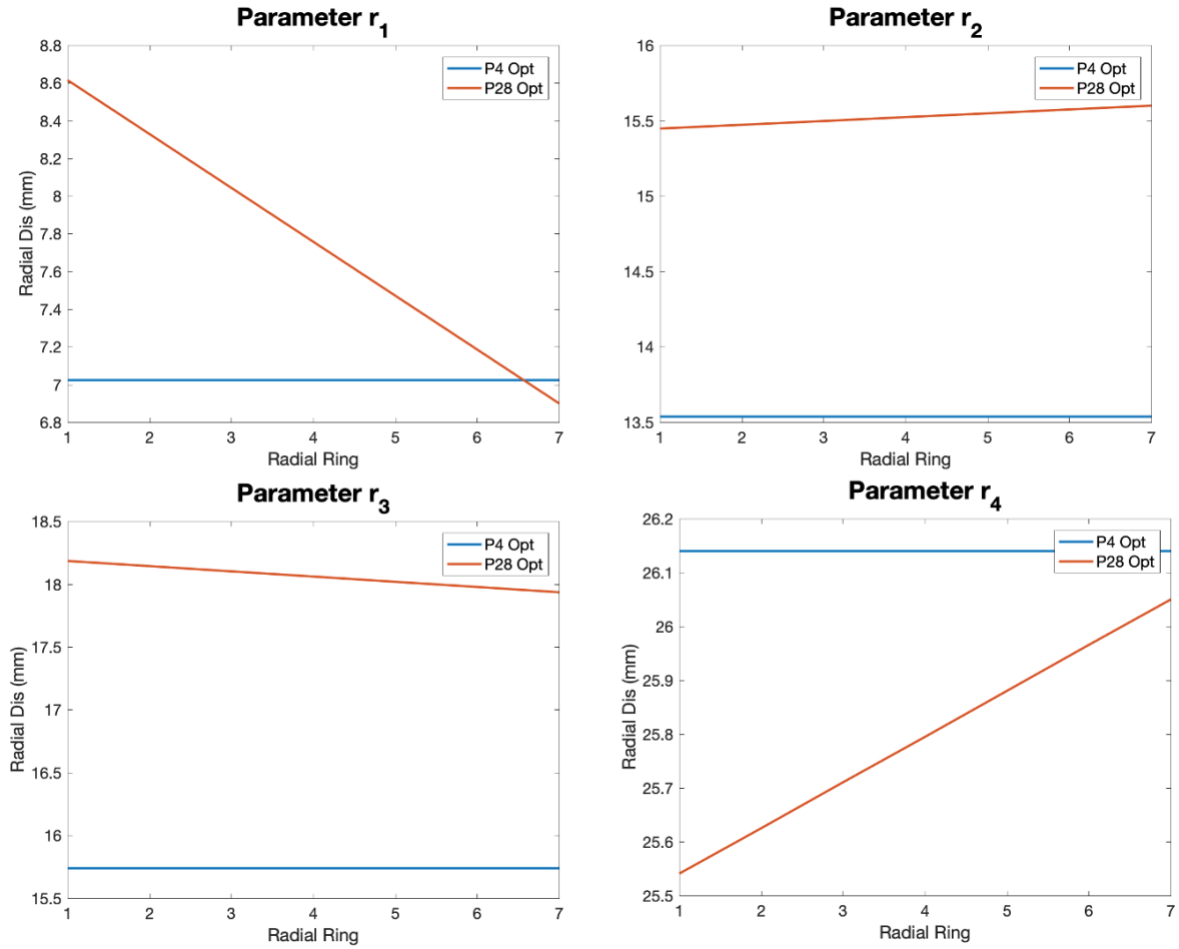

Figure 14. Core radial parameter variation in the 28-parameter optimization. The blue horizontal lines show the optimized baseline values.

Figure 14 shows the differences in geometry parameters of the baseline and radially optimized designs. Parameter R1 controls the inner hole of the YH moderator rod. This parameter experiences the most radial variation with the largest holes being in the center of the core tapering off to the edge. Another parameter with large radial variation is R4, which controls the cooling channel between cogs. The smaller this parameter is, the larger the cooling channel becomes. It can be seen that R4 for the radially optimized design is ~0.7mm lower for radial zone 1 and ~0.1mm lower for radial zone 7, which translates into a 1.4mm larger cooling channel in zone 1 and 0.2mm larger channel in zone 7. Parameters R2 and R3 have little variation and their shift from the baseline design directly leads to reduction in total fuel and moderator volume.

The stability of the optimized design to manufacturing and assembly tolerances is evaluated below. The figures in this section demonstrate the stability of the radially optimized design with respect to variation in the geometric parameters. This is important for analyzing the manufacturing and core assembly dimensional uncertainties that affect the core performance. Figure 15 shows a simulation where the design parameters are within a tolerance of 2 mm from the optimal design. The result demonstrates how tolerances of more than 1mm can change the performance of the reactor core. The difference is visually apparent in the temperature plots of Figure 15 (last row), where the loss function increases from 14.7℃ to 32.4℃.

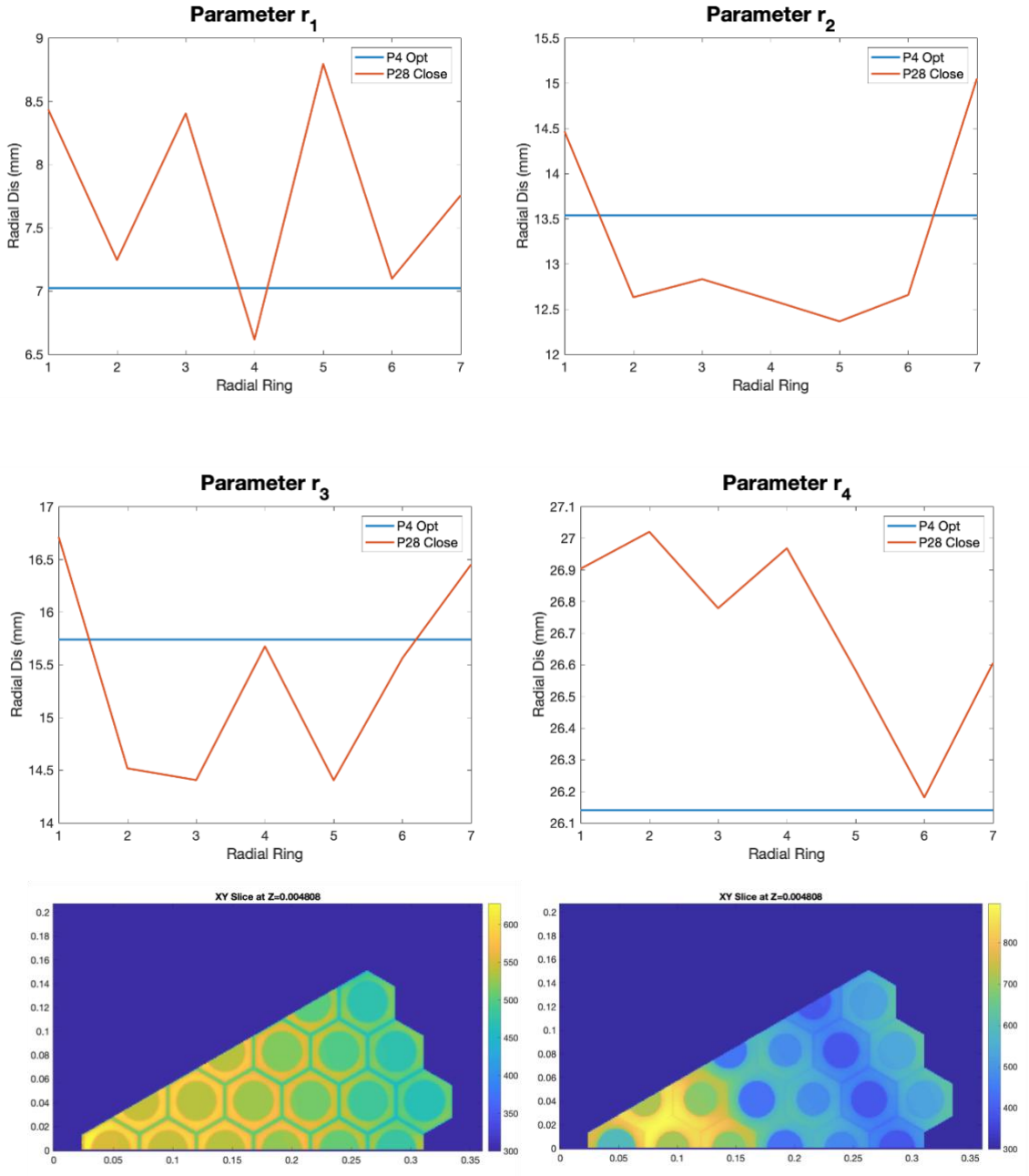

Figure 15. ***Top two rows*****: The blue horizontal lines show the optimized baseline values. The red lines depict the closest 28 parameter design to the optimized baseline in the database of simulated models.** ***Bottom row*****: Temperature distribution of blue parameter design on the left and red parameters on the right.**

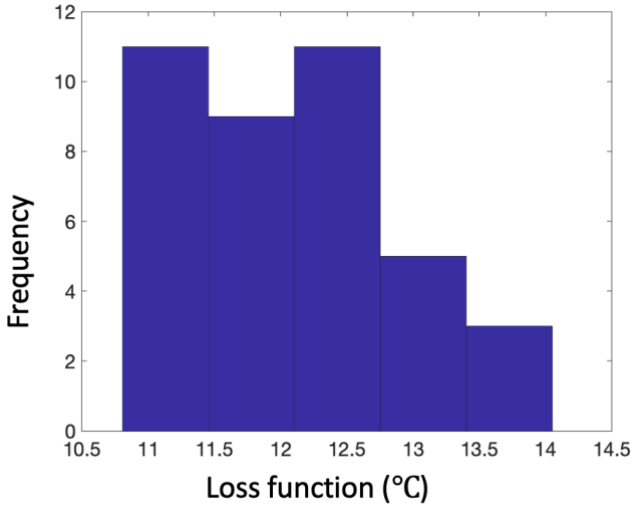

Figure 16. All 38 designs within a 1mm of optimum have low loss function, ranging from 10.8C to 14C.

Figure 16 indicates the stability of the radially optimized design, achieved in this work. In the optimization process, 38 designs were analyzed using high fidelity simulations where the parameters are within less than 1mm of the final, optimal design. Figure 16 shows the distribution of the loss function for all 38 designs that were close to the optimum. The loss function variation is between 10.8°C and 14°C. This is much less than the value of 32.4 C, when the manufacturing tolerances exceed 1 mm.

It must be noted that more needs to be done to strengthen this statement about stability. All 38 designs were obtained near the end of the optimization route, when the algorithm had learned to find the optimal designs by running high fidelity simulation. Further studies must be done, and the algorithm is to be modified to choose the worst-case designs near the optimum. More high-fidelity simulations must be performed near the optimized design, which will improve our ability to predict stability.

Figure 17 illustrates the method's ability to reveal interesting characteristics of the design space. It is seen on the left that unique, dynamic, temperature patterns can occur when parameters are randomly modified. The algorithm discovered that designs exist that produce diverse different hot and cold areas in the core.

The correct heat distribution in the core maintains an optimum loss function of 11.2°C if the spacing between cogs is increased, relative to the baseline design. This design has a minimum cooling channel width of 2.5mm, allowing for greater manufacturing tolerance in cog placement to be accommodated.

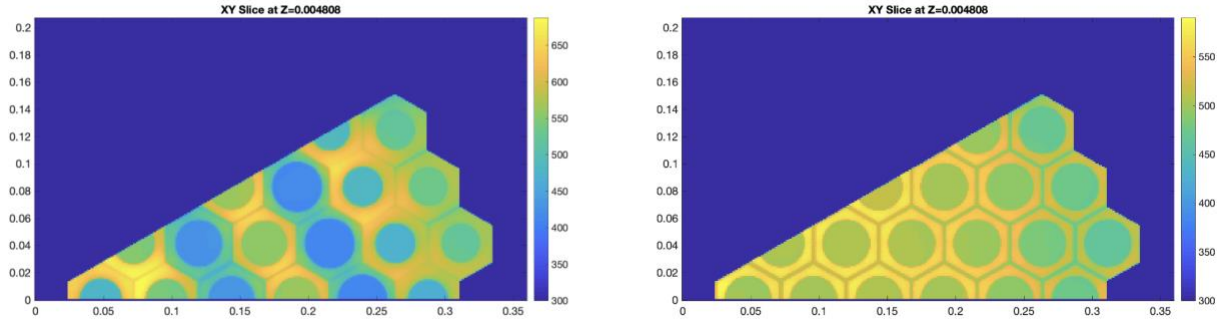

Figure 17. Left - Design that demonstrates the ability to distribute temperature in the core. Right - Design that provides a minimum of 2.5mm of spacing between each cog with a loss function of 11.2C.

4. CONCLUSIONS AND DISCUSSION

This report presents the results for the AI-based design optimization of a full nuclear reactor core with variable assembly design with the objective of minimizing the thermal-induced mechanical stress. To accelerate the optimization space search, the authors developed an ML-based multiphysics emulator capable of running efficiently on Summit. This work demonstrated how an AI-based optimization algorithm can efficiently sample the vast and continuous search space of arbitrary geometry to find the optimal solution with significant performance improvement.

The natural progression of the challenge problem established in this report is to expand the parameter space to allow axial variation in the four parameters controlling the thickness of the moderator, fuel, and cooling channels. As observed in Figure 10, the largest amount of temperature variation in any single core element is predicted to occur at the bottom of the core. As demonstrated in Section 3.1, progress under the TCR program has yielded the technical capability to model axial variation, and the authors have shown that it can significantly improve reactor core performance.

The authors envision a rapidly developing and promising future for nuclear systems design with arbitrary geometry. Arbitrary geometry enabled through advanced manufacturing provides a vast variety of unexplored opportunities in nuclear system design. Historically, many engineering objectives in nuclear reactor design were met through creative combinatorial solutions of fuel loading axially and radially. Arbitrary geometry allows researchers to explore alternative solutions to these engineering challenges. Furthermore, combining variable fuel loading with elements of arbitrary geometry to maximize nuclear reactor safety and economics is an exciting opportunity.

The second exciting opportunity that could result from this work is the rapid design evolution that can be achieved with ML-based surrogate models, as presented in this work. This work demonstrated that it is possible to construct ML-based surrogate models capable of capturing a large percentage of the system physics but that can be evaluated to predict the performance of candidate designs at a fraction of the computational time. This step is absolutely necessary for searching larger and larger design spaces that allow for more complex nuclear system geometries.

AI-based nuclear systems design is not anticipated to completely replace human designers; rather, AI-based design is expected to become one of the primary tools of the human designer. In this case, the way in which engineers think about the design problem must shift. The new focus must be to carefully craft the parameters of the optimization problem and establish the objective and constraints. The accurate formulation of the objectives will be vital, especially finding the right balance between multiple objectives. The parameters of the optimization must be chosen very carefully to reduce the possible design space as much as possible while maintaining enough flexibility to allow for significant performance improvements.

Although many challenges undoubtedly still remain, the combination of (1) arbitrary geometry enabled by advanced manufacturing, (2) ML-based surrogate models for fast and predictive computational evaluation, and (3) AI-based optimization algorithms form a very exciting future for nuclear design. This combination has the potential to discover revolutionary changes in the safety, efficiency, and economy of nuclear systems, helping contribute to safer and cleaner energy for the world.

5. REFERENCES

1. Jared, Bradley H., Miguel A. Aguilo, et al. 2017. "Additive Manufacturing: Toward Holistic Design." *Scripta Materialia* 135: 141–147. https://doi.org/10.1016/j.scriptamat.2017.02.029. http://www.sciencedirect.com/science/article/pii/S1359646217300957.
2. Thompson, Mary Kathryn, Giovanni Moroni, et al. 2016. "Design for Additive Manufacturing: Trends, Opportunities, Considerations, and Constraints." *CIRP Annals* 65 (2): 737–760. https://doi.org/10.1016/j.cirp.2016.05.004. http://www.sciencedirect.com/science/article/pii/S0007850616301913.
3. Tobin, K. W., J. T. Busby, et al. 2018. *Technologies to Reactors: Enabling Accelerated Deployment of Nuclear Energy Systems Workshop Report.* Oak Ridge National Laboratory (United States), ORNL/SPR-2018/1025. https://www.osti.gov/servlets/purl/1490719.
4. Sobes, Vladimir, Briana Hiscox, et al. 2021. "Artificial Intelligence Design of Nuclear Systems Empowered by Advanced Manufacturing." EPJ Web of Conferences.
5. Sobes, V., B. D. Hiscox, et al. 2020. "Artificial Intelligence Design of Nuclear Systems Empowered by Advanced Manufacturing." PHYSOR 2020 – Transition to a Scalable Nuclear Future, Cambridge, United Kingdom.
6. Ade, Brian J., Benjamin R. Betzler, et al. 2021. "Candidate Core Designs for the Transformational Challenge Reactor." *Journal of Nuclear Engineering* 2 (1). https://doi.org/10.3390/jne2010008.
7. Betzler, Benjamin R, Brian J Ade, et al. 2021. "Advanced Manufacturing for Nuclear Core Design." EPJ Web of Conferences.
8. Betzler, B. R., B. J. Ade, et al. 2018. *Transformational Challenge Reactor Preconceptual Design Incorporating Rapid Prototyping Via Advanced Manufacturing.* Oak Ridge National Laboratory, ORNL/SPR-2018/1008.
9. Betzler, B. R., B. J. Ade, et al. 2020. "Advanced Manufacturing for Nuclear Core Design." PHYSOR 2020 – Transition to a Scalable Nuclear Future, Cambridge, United Kingdom.
10. "Transformational Challenge Reactor." 2019. Oak Ridge National Laboratory. Accessed Dec. 1. https://tcr.ornl.gov/.
11. Hehr, Adam, Justin Wenning, et al. 2017. "Five-Axis Ultrasonic Additive Manufacturing for Nuclear Component Manufacture." *JOM* 69 (3): 485–490. https://doi.org/10.1007/s11837-016-2205-6. https://doi.org/10.1007/s11837-016-2205-6.
12. Gomez-Fernandez, Mario, Kathryn Higley, et al. 2020. "Status of Research and Development of Learning-Based Approaches in Nuclear Science and Engineering: A Review." *Nuclear Engineering and Design* 359: 110479. https://doi.org/https://doi.org/10.1016/j.nucengdes.2019.110479. https://www.sciencedirect.com/science/article/pii/S0029549319305102.
13. Radaideh, Majdi I, Dean Price, and Tomasz Kozlowski. 2021. "Modeling Nuclear Data Uncertainties Using Deep Neural Networks." EPJ Web of Conferences.
14. Grechanuk, Pavel A, Michael E Rising, and Todd S Palmer. 2021. "Application of Machine Learning Algorithms to Identify Problematic Nuclear Data." *Nuclear Science Engineering*: 1-14.

15. Talou, Patrick. 2021. "Making Sense of Uncertain Nuclear Data." *Annals of Nuclear Energy* 164: 108568.
16. Herman, M, DA Brown, et al. 2020. "New Paradigm for Nuclear Data Evaluation." EPJ Web of Conferences.
17. Sobes, Vladimir, Michael Grosskopf, et al. 2020. *Wanda: Ai/Ml for Nuclear Data.* Oak Ridge National Lab.(ORNL), Oak Ridge, TN (United States).
18. Vicente-Valdez, Pedro, Lee Bernstein, and Massimiliano Fratoni. 2021. "Nuclear Data Evaluation Augmented by Machine Learning." *Annals of Nuclear Energy* 163: 108596.
19. Alamaniotis, Miltiadis, and Alexander Heifetz. 2022. "Survey of Machine Learning Approaches in Radiation Data Analytics Pertained to Nuclear Security." In *Advances in Machine Learning/Deep Learning-Based Technologies: Selected Papers in Honour of Professor Nikolaos G. Bourbakis – Vol. 2*, edited by George A. Tsihrintzis, Maria Virvou and Lakhmi C. Jain, 97-115. Cham: Springer International Publishing.
20. Kropaczek, David J., and Paul J. Turinsky. 1991. "In-Core Nuclear Fuel Management Optimization for Pressurized Water Reactors Utilizing Simulated Annealing." *Nuclear Technology* 95 (1): 9-32. https://doi.org/10.13182/NT95-1-9. https://doi.org/10.13182/NT95-1-9.
21. Turinsky, Paul J. 2005. "Nuclear Fuel Management Optimization: A Work in Progress." *Nuclear Technology* 151 (1): 3-8. https://doi.org/10.13182/NT05-A3626. https://doi.org/10.13182/NT05-A3626.
22. Nissan, Ephraim. 2019. "An Overview of Ai Methods for in-Core Fuel Management: Tools for the Automatic Design of Nuclear Reactor Core Configurations for Fuel Reload,(Re) Arranging New and Partly Spent Fuel." *Designs* 3 (3): 37.
23. da Silva, Márcio Henrique, and Roberto Schirru. 2011. "Optimization of Nuclear Reactor Core Fuel Reload Using the New Quantum Pbil." *Annals of Nuclear Energy* 38 (2-3): 610-614.
24. Huang, Lloyd Michael. 2017. "Neutronic Analysis and Optimization of the Advanced High Temperature Reactor Fuel Design Using Machine Learning." Georgia Institute of Technology.
25. Li, Zeguang, Jun Sun, et al. 2020. "A New Cross-Section Calculation Method in Htgr Engineering Simulator System Based on Machine Learning Methods." *Annals of Nuclear Energy* 145: 107553.
26. Kwapis, Emily H, Hongcheng Liu, and Kyle C Hartig. 2021. "Tracking of Individual Triso-Fueled Pebbles through the Application of X-Ray Imaging with Deep Metric Learning." *Progress in Nuclear Energy* 140: 103913.
27. Zeguang, LI, Jun Sun, et al. 2021. "Research on the Cross-Section Generating Method in Htgr Simulator Based on Machine Learning Methods." EPJ Web of Conferences.
28. Turkmen, Mehmet, Gwendolyn JY Chee, and Kathryn D Huff. 2021. "Machine Learning Application to Single Channel Design of Molten Salt Reactor." *J Annals of Nuclear Energy* 161: 108409.
29. Betzler, Benjamin R., David Chandler, et al. 2019. "Design Optimization Methods for High-Performance Research Reactor Core Design." *Nuclear Engineering and Design* 352: 110167. https://doi.org/10.1016/j.nucengdes.2019.110167. http://www.sciencedirect.com/science/article/pii/S0029549319301773.

30. Do, Binh Quang, and Lan Phuoc Nguyen. 2007. "Application of a Genetic Algorithm to the Fuel Reload Optimization for a Research Reactor." *Applied Mathematics Computation* 187 (2): 977-988.
31. Kim, Song Hyun, Sung Gyun Shin, et al. 2020. "Feasibility Study on Application of an Artificial Neural Network for Automatic Design of a Reactor Core at the Kyoto University Critical Assembly." *Progress in Nuclear Energy* 119: 103183.
32. Wahed, Mohamed E, and Wesam Z Ibrahim. 2010. "Neural Network and Genetic Algorithms for Optimizing the Plate Element of Egyptian Research Reactor Problems." *Nuclear engineering design* 240 (1): 191-197.
33. International, Nuclear Engineering. 2021. "Westinghouse Produces 3d-Printed Component for Us Nuclear Plant."
34. Nelson, Andrew. 2019. *Features That Further Performance Limits of Nuclear Fuel Fabrication: Opportunities for Additive Manufacturing of Nuclear Fuels.* Oak Ridge National Lab.(ORNL), Oak Ridge, TN (United States).
35. Yang, Jae Ho, Dong Seok Kim, et al. 2021. "A Feasibility Study on the Application of Additive Manufacturing Method to Fabricate Nuclear Fuel Using Surrogate."
36. Bergeron, A., and J. B. Crigger. 2018. "Early Progress on Additive Manufacturing of Nuclear Fuel Materials." *Journal of Nuclear Materials* 508: 344-347. https://doi.org/https://doi.org/10.1016/j.jnucmat.2018.05.058. https://www.sciencedirect.com/science/article/pii/S0022311518306780.
37. Rosales, Jhonathan, Isabella J van Rooyen, and Clemente J %J Journal of Nuclear Materials Parga. 2019. "Characterizing Surrogates to Develop an Additive Manufacturing Process for U3si2 Nuclear Fuel." 518: 117-128.
38. Singamneni, Sarat, Yifan Lv, et al. 2019. "Additive Manufacturing for the Aircraft Industry: A Review." 8: 1. https://doi.org/10.4172/2329-6542.1000214.
39. Terrani, K. A., B. C. Jolly, et al. 2021. "Architecture and Properties of Tcr Fuel Form." *Journal of Nuclear Materials*: 152781. https://doi.org/https://doi.org/10.1016/j.jnucmat.2021.152781. http://www.sciencedirect.com/science/article/pii/S0022311521000040.
40. Trammell, M. P., Brian C. Jolly, et al. 2019. *Advanced Nuclear Fuel Fabrication: Particle Fuel Concept for Tcr.* Oak Ridge National Laboratory (Oak Ridge, Tennessee, USA), ORNL/SPR-2019/1216, M3CT-19OR06090130.
41. Sobes, Vladimir, Briana Hiscox, et al. 2021. "Artificial Intelligence Design of Nuclear Systems Empowered by Advanced Manufacturing*." *EPJ Web Conf.* 247. https://doi.org/10.1051/epjconf/202124706032.
42. Pevey, J., and et. al. (submitted) 2021. "Gradient-Informed Design Optimization of Nuclear Systems." *Nuclear Science and Engineering*.
43. Popov, E., and et. al. (submitted) 2022. "Artificial Intelligence Driven Additive Manufactured Reactor Thermal-Hydraulics Design." International Topical Meeting on Nuclear Reactor Thermal Hydraulics, Brussels, Belgium.
44. Sobes, V., and et. al. (in review) 2021. "Ai-Based Design of a Nuclear Reactor Core." *Nature Scientific Reports*.
45. Facility, Oak Ridge Leadership Computing. 2021. "Summit: America's Newest and Smartest Supercomputer." www.olcf.ornl.gov/Summit/.
46. Forrester, Alexander, Andras Sobester, and Andy Keane. 2008. *Engineering Design Via Surrogate Modelling: A Practical Guide*. John Wiley & Sons.

47. Goorley, J.T., et al. 2013. *Initial Mcnp6 Release Overview - Mcnp6 Version 1.0.* Los Alamos National Laboratory (Los Alamos, New Mexico, USA), LA-UR-13-22934. https://laws.lanl.gov/vhosts/mcnp.lanl.gov/pdf_files/la-ur-13-22934.pdf.
48. Team, X. Monte Carlo. 2003. *Mcnp - Version 5, Vol. I: Overview and Theory.* Los Alamos National Laboratory (Los Alamos, New Mexico, USA), LA-UR-03-1987. https://mcnp.lanl.gov/pdf_files/la-ur-03-1987.pdf.
49. Siemens. 2021. "Simcenter Star-Ccm+ Software." https://www.plm.automation.siemens.com/global/en/products/simcenter/STAR-CCM.html.
50. ANSYS, Inc. 2009. *Ansys-12.0 Theory Guide.*

APPENDIX A. INLET FLOW STRUCTURE OPTIMIZATION

A-1. INLET PLENUM DESIGN SPACE SENSITIVITY STUDY

One of the first steps of a robust design optimization study is to perform a design space sensitivity analysis. A design space sensitivity analysis allows the various design parameters to be manipulated, often to extremes, to determine how sensitive they are to the design objectives. Then, only the variables proven to be sensitive to the design's objectives are used in the design optimization study. This process is usually automated; however, it was conducted by hand for the pressure vessel's inlet plenum.

A-1.1 Background and Baseline Design

Initial estimates for the allowable system-level pressure loss across the pressure vessel and core were roughly one-tenth of an atmosphere, or 1.4 psi. Therefore, a detailed design study was required to understand the nature of the pressure loss in the inlet plenum and optimize the geometry to reduce the total pressure loss from the pressure vessel inlet through the inlet to the core located at the top reflectors, as shown in Figure A-1. This overall pressure loss reduction gives the TCR core design team more design space for its efforts.

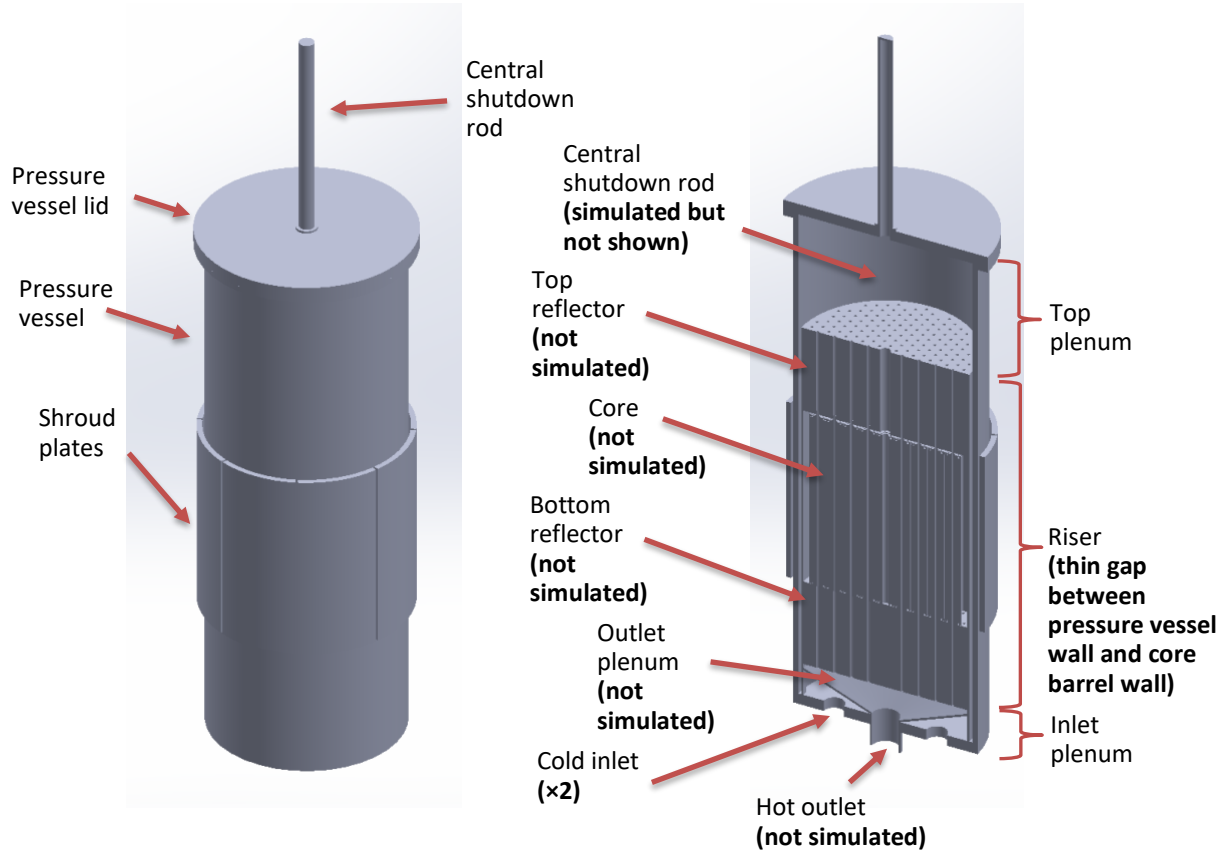

Figure A-1. Baseline simulation geometry.

Beyond the pressure losses, two additional design goals were determined to reduce and/or mitigate any potential hot spots in the riser section and ensure that coolant flow within the top plenum efficiently translates from riser section to the inlets of the top reflectors.

To accomplish these goals, the computational fluid dynamic software STAR-CCM+ was used. The Reynolds-averaged Navier-Stokes coupled energy/flow solver was used with Mentor's K-Omega turbulence model and Siemens' Low y+ wall treatment. All solutions were run until monitor residuals and key parameters converged.

The overall pressure drop of the baseline system was approximately 0.8 psid, which represents 57% of the allowable limit for the entire pressure vessel and core. As shown in Figure A-2 and Table A-1, most of the pressure drop is created in the inlet plenum where the inlet flow enters the system and directly makes contact with the structural funnel of the outlet plenum.

Figure A-2. Total pressure contour of baseline geometry.

Table A-1. Breakdown of total pressure drop across baseline geometry.

Location	P_{Total} (psi)	ΔP_T (psi)	System ΔP_T (psi) (outlet–inlet)
Inlet	1.016175e+03		
Riser section, inlet	1.015669e+03	-0.506	
Riser section, outlet	1.015561e+03	-0.108	
Outlet	1.015376e+03	-0.185	-0.799

To evaluate and mitigate any hot spots in the riser section, the uniformity of the coolant velocity vertical component was monitored. The formation of hot spots on the core barrel is directly affected by the efficiency of the convective cooling. Nonuniform flow fields will directly relate to nonuniform cooling and the formation of hot spots. Figure A-3 and Table A-2 show the current state of the vertical flow uniformity in the baseline geometry.

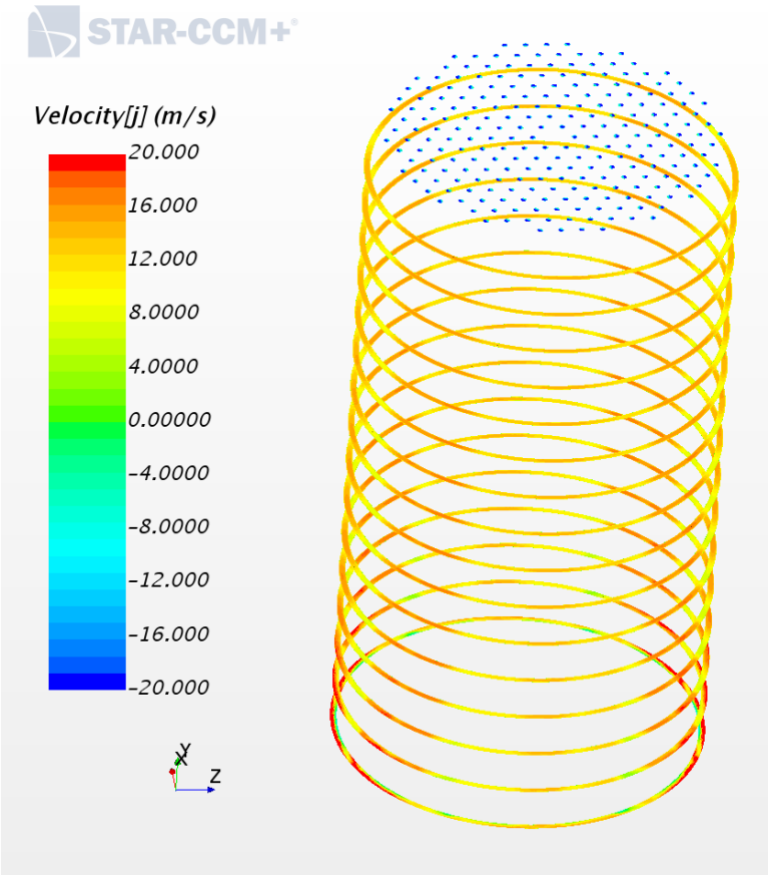

Figure A-3. Vertical velocity contours in riser section of baseline geometry.

Table A-2. Vertical velocity uniformity vs. vertical location within baseline geometry.

Location	Uniformity, velocity, *y* (%)	Average velocity, *y* (m/s)	Standard deviation velocity, *y* (m/s)
Riser section, inlet: *y* = 0.2 m	75.44655	12.71377	8.555479
y = 0.3 m	86.09353	12.69891	4.414562
y = 0.4 m	87.90012	12.70462	3.594079
y = 0.5 m	88.91442	12.71372	3.305879
y = 0.6 m	89.61445	12.72582	3.145427
y = 0.7 m	90.16956	12.73518	3.025233
y = 0.8 m	90.64227	12.74169	2.917934
y = 0.9 m	91.05152	12.74670	2.819611
y = 1.0 m	91.41974	12.75226	2.725472
y = 1.1 m	91.74658	12.75238	2.632681
y = 1.2 m	92.07276	12.75169	2.541138
y = 1.3 m	92.38742	12.75020	2.453745
y = 1.4 m	92.69964	12.74072	2.367193
y = 1.5 m	92.99845	12.73100	2.285984
y = 1.6 m	93.28052	12.72638	2.210257
Riser section, outlet: *y* = 1.7 m	93.54476	12.72783	2.137942
Reflector channels: *y* = 1.8 m	83.40037	-15.84050	6.201386

Several large eddies form within the top plenum. These recirculating regions cause the coolant flow to pass the inlets to the top reflectors at a near-tangential vector. A vector normal to the entrance plane is desired because it encourages coolant to flow smoothly from the inlet down into the core and not cause stagnate pockets of recirculating coolant within the top plenum. Figure A-4 shows the coolant flow paths within the top plenum of the baseline geometry.

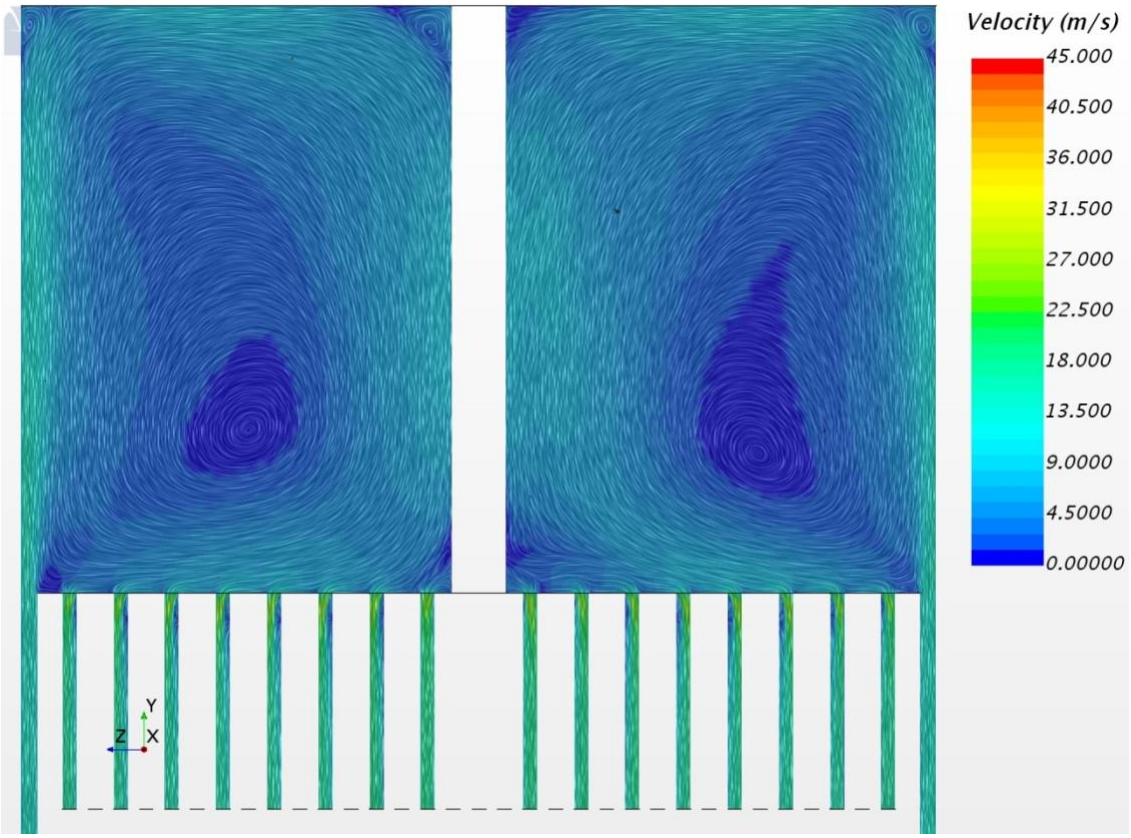

Figure A-4. Coolant flow paths within the top plenum of the baseline geometry.

Simulating the baseline geometry shows that the flow path within the inlet plenum must be modified to eliminate high-pressure losses. Additional attention is required to ensure that future modification attempts create greater uniformity of the vertical flow within the riser section and enhance the flow patterns within the top plenum.

A-1.2 Inlet Plenum Design Modification 1

In the first attempt to reduce pressure losses within the inlet plenum, the over height of the inlet plenum was increased by 5 in., and the two vessel inlet tubes were moved further outboard near the pressure vessel wall. This mitigated the need for the inlet flow to transition outboard within the inlet plenum before entering the riser section. Next, the freedom of design lent by additive manufacturing was used, and an internal duct was created with a smother geometric transition between the smaller circular inlet tubes and the anulus shape of the riser section. Figure A-5 and Figure A-6 provide additional details.

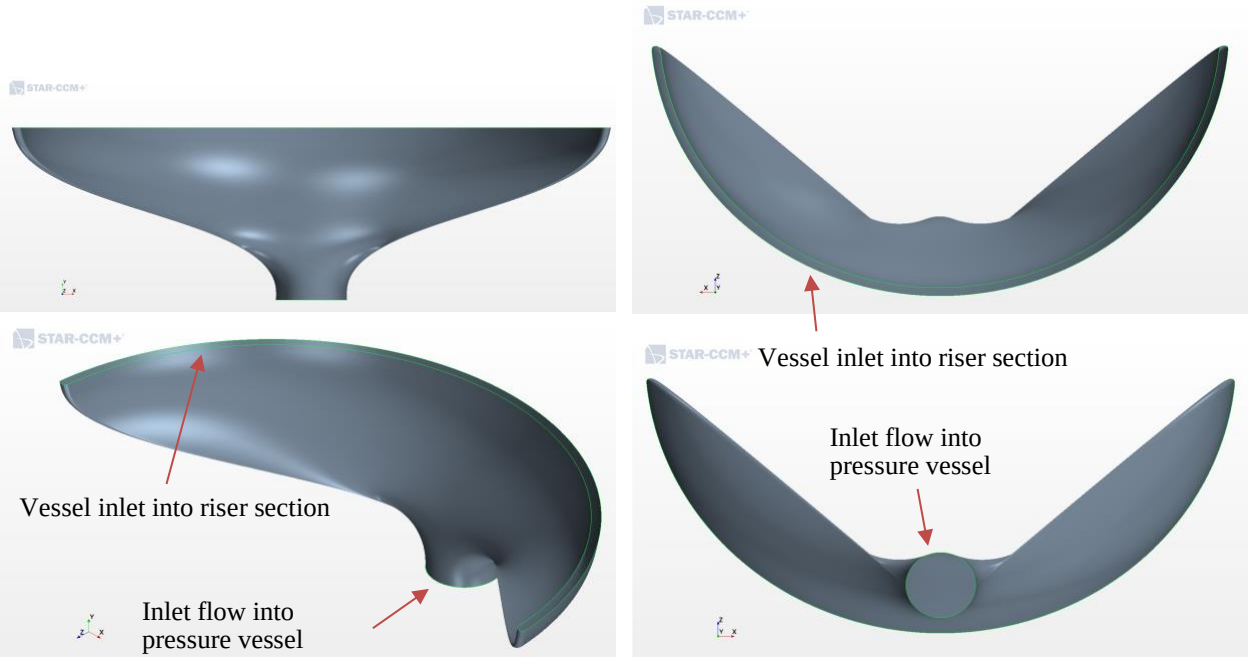

Figure A-5. Various views of the inlet ducting geometry.

Figure A-6. Inlet plenum design modification 1 geometry.

The overall pressure drop savings for the system were reduced to approximately 0.43 psid, or a 54.9% savings with respect to the baseline geometry. This represents 30.1% of the total allowable limit for the entire system. Table A-3 provides additional details.

Table A-3. Breakdown of total pressure drop across design modification 1 geometry.

Location	P_{Total} (psi)	ΔP_T (psi)	System ΔP_T (psi) (outlet–inlet)
Inlet	1.015749e+03		
Riser section, inlet	1.015675e+03	-0.074	
Riser section, outlet	1.015574e+03	-0.101	
Outlet	1.015381e+03	-0.193	-0.368

Although the pressure drop improved, the vertical velocity uniformity within the riser section worsened. This was caused by an uneven flow distribution within the inlet duct, leading to a large area of reverse flow within the riser section. Table A-4, Figure A-7, and Figure A-8 provide specific details.

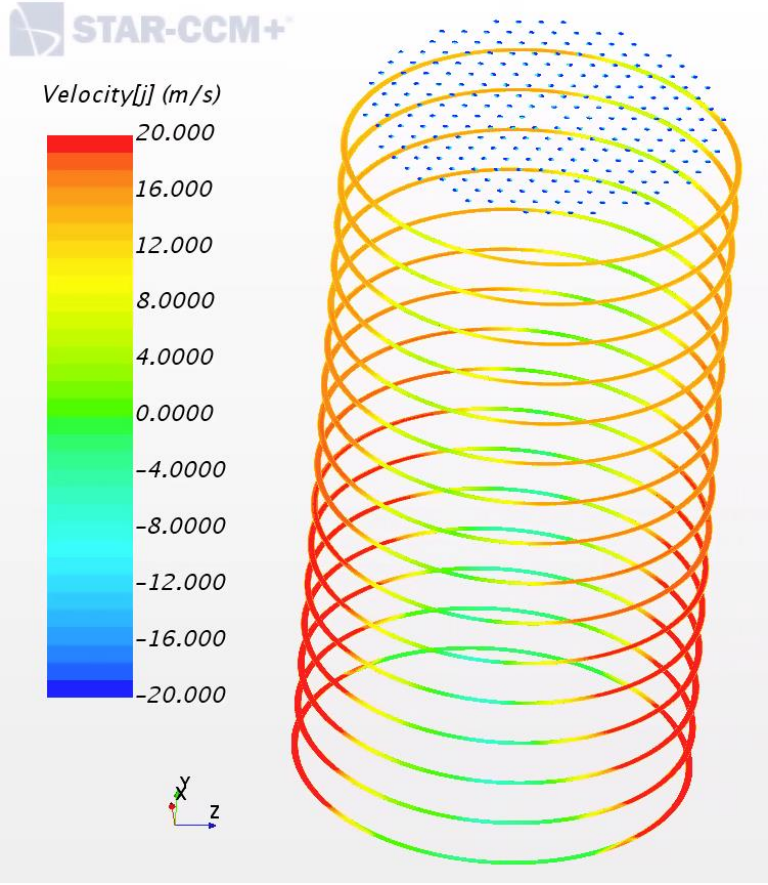

Figure A-7. Vertical velocity contours in riser section of design modification 1 geometry.

Table A-4. Vertical velocity uniformity vs. vertical location within design modification 2 geometry.

Location	Uniformity, velocity *y* (%)	Average velocity *y* (m/s)	Standard deviation velocity *y* (m/s)
Riser section, inlet: *y* = 0.2 m	54.49909	12.73166	12.69475
y = 0.3 m	59.92011	12.74439	11.25646
y = 0.4 m	63.87391	12.73069	10.24041
y = 0.5 m	67.37308	12.73041	9.414526
y = 0.6 m	71.13959	12.79508	8.483388
y = 0.7 m	74.23953	12.80089	7.642588
y = 0.8 m	76.82425	12.77239	6.816371
y = 0.9 m	78.99048	12.73076	6.140047
y = 1.0 m	80.77159	12.67978	5.652304
y = 1.1 m	82.67646	12.67537	5.144141
y = 1.2 m	84.33894	12.66534	4.681661
y = 1.3 m	85.72365	12.64729	4.275317
y = 1.4 m	86.93220	12.64441	3.931898
y = 1.5 m	88.10937	12.72607	3.618296
y = 1.6 m	89.26571	12.72607	3.320252
Riser section, outlet: *y* = 1.7 m	90.19864	12.76592	3.072772
Reflector channels: *y* = 1.8 m	86.82995	-16.20756	5.157363

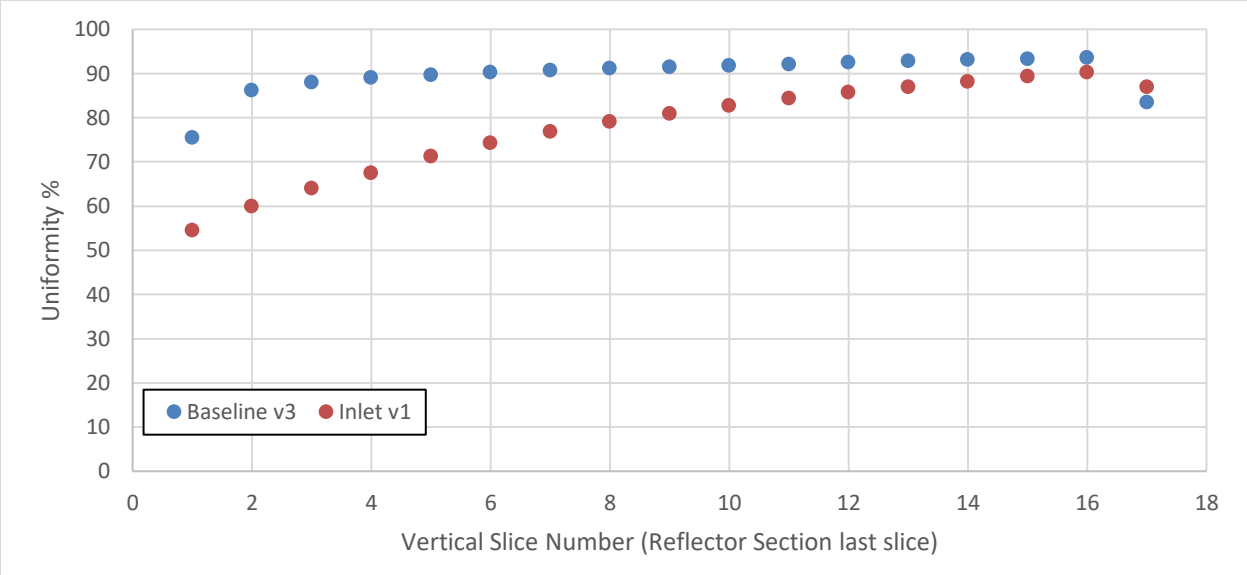

Figure A-8. Uniformity of riser section vertical velocity.

The newly designed inlet ducts did not cause many changes within the top plenum; several large eddies still dominate the flow, resulting in a near-tangential inlet angle at the top reflectors. However, the flow has obtained a rotational quality about the shutdown rod. Figure A-9 and Figure A-10 provide additional details.

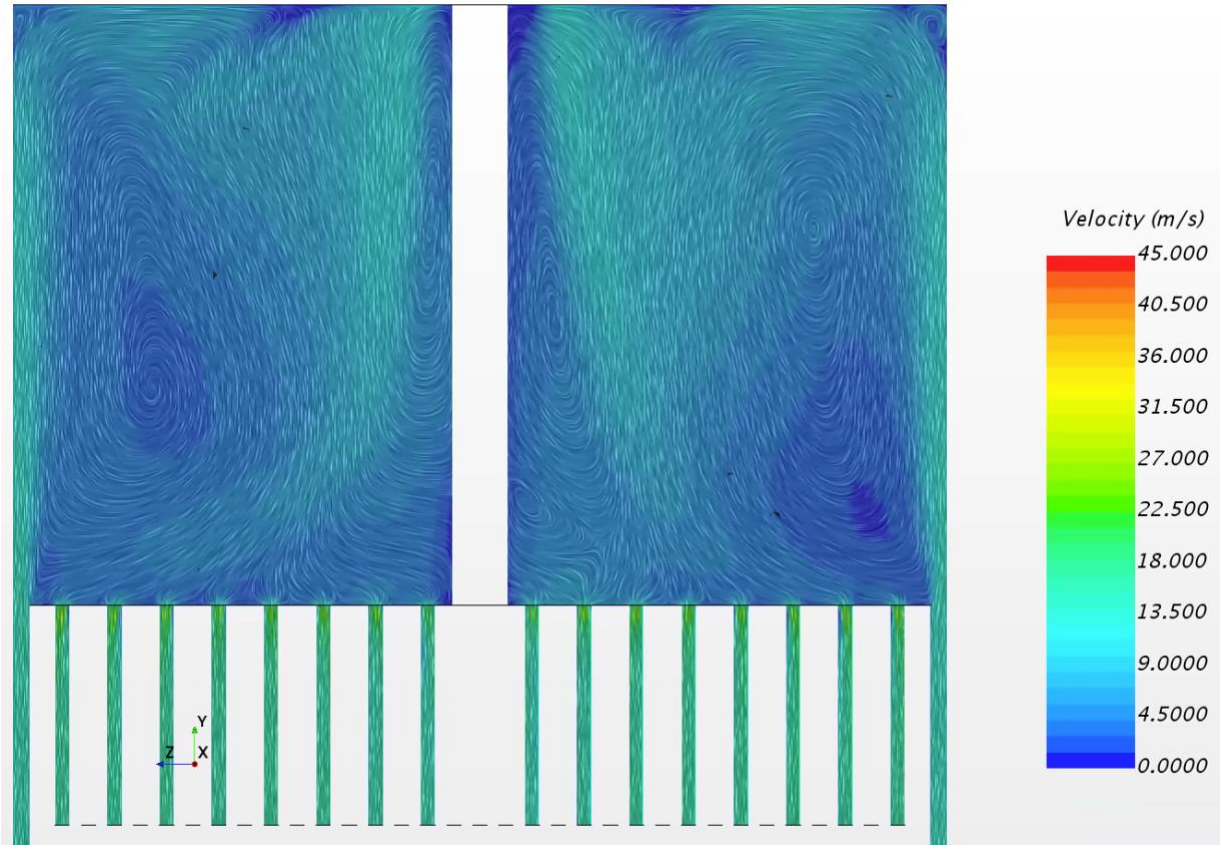

Figure A-9. Coolant flow paths within the top plenum of design modification 1 geometry.

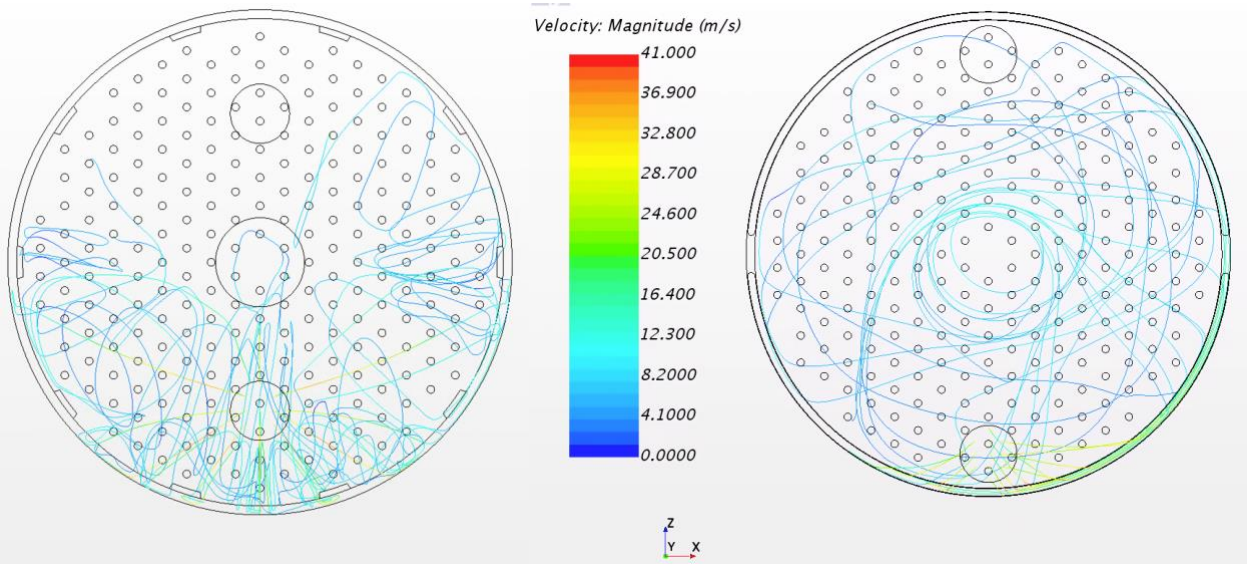

Figure A-10 Streamlines of coolant flow paths within the top plenum: baseline geometry (left) and design modification 1 geometry (right).

Although the pressure drop caused by the inlet plenum was drastically reduced, the resulting effect was a reduction in vertical velocity uniformity within the riser section. Further designs were needed to address this loss in uniformity while maintaining, or further reducing, the system pressure losses.

A-1.3 Inlet Plenum Design Modification 2

As a second attempt to reduce pressure losses within the inlet plenum while gaining back the lost velocity uniformity within the riser section, the overall height of the inlet plenum was increased by 24 in. Figure A-11 and Figure A-12 provide additional details.

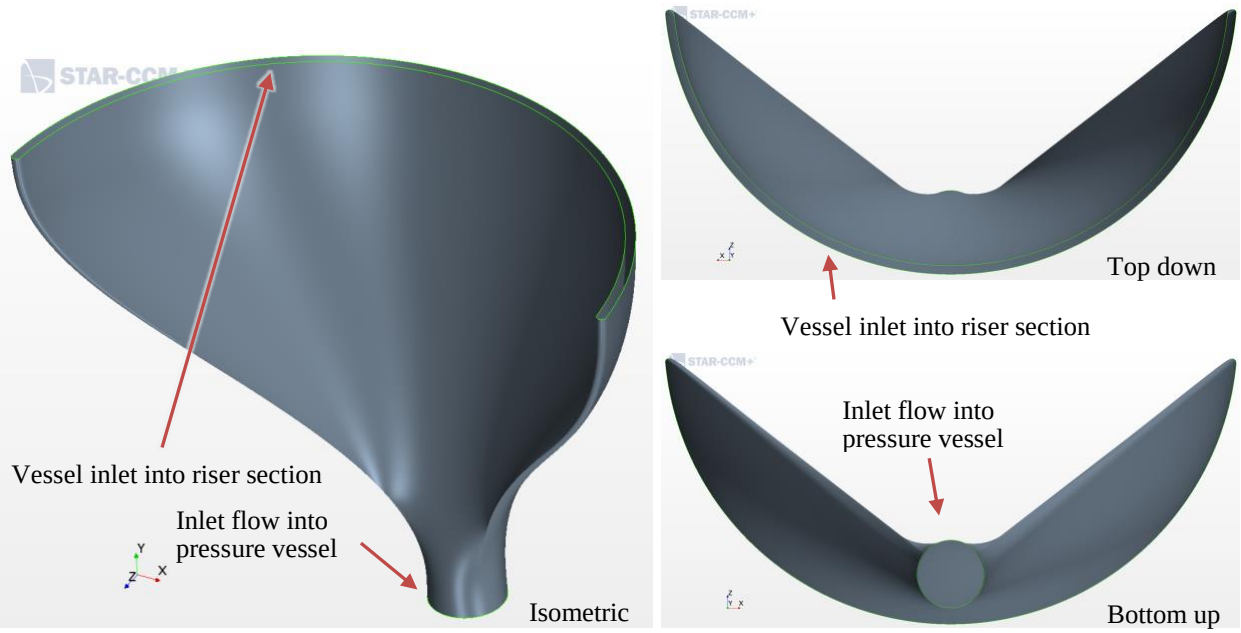

Figure A-11. Various views of the design modification 2 inlet ducting geometry.

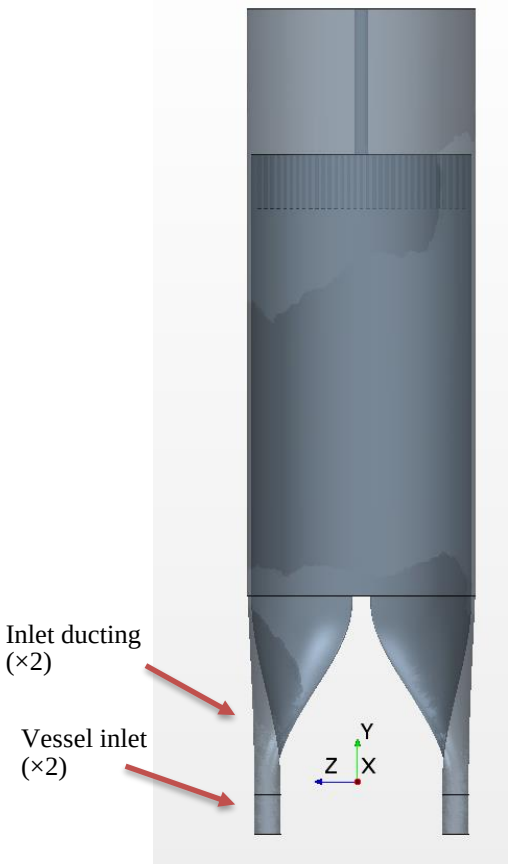

Figure A-12. Inlet plenum design modification 2 geometry.

The overall pressure drop savings for the system were further reduced to approximately 0.36 psid, which represents 25.4% of the total allowable limit for the entire system. This confirms that the added height of the inlet duct helped further create a smooth transition between the vessel inlets and the riser section. Table A-5 provides additional details.

Table A-5. Breakdown of total pressure drop across design modification 2 geometry.

Location	P_{Total} (psi)	ΔP_T (psi)	System ΔP_T (psi) (outlet–inlet)
Inlet	1.015737e+03		
Riser section, inlet	1.015649e+03	-0.088	
Riser section, outlet	1.015569e+03	-0.080	
Outlet	1.015382e+03	-0.187	-0.355

The velocity uniformity within the riser section gained back some of its uniformity with the increased duct geometry height. However, more must be done to further spread the flow evenly within the inlet duct that leads to the riser section. Table III, Figure 18, and Figure 19 provide specific details.

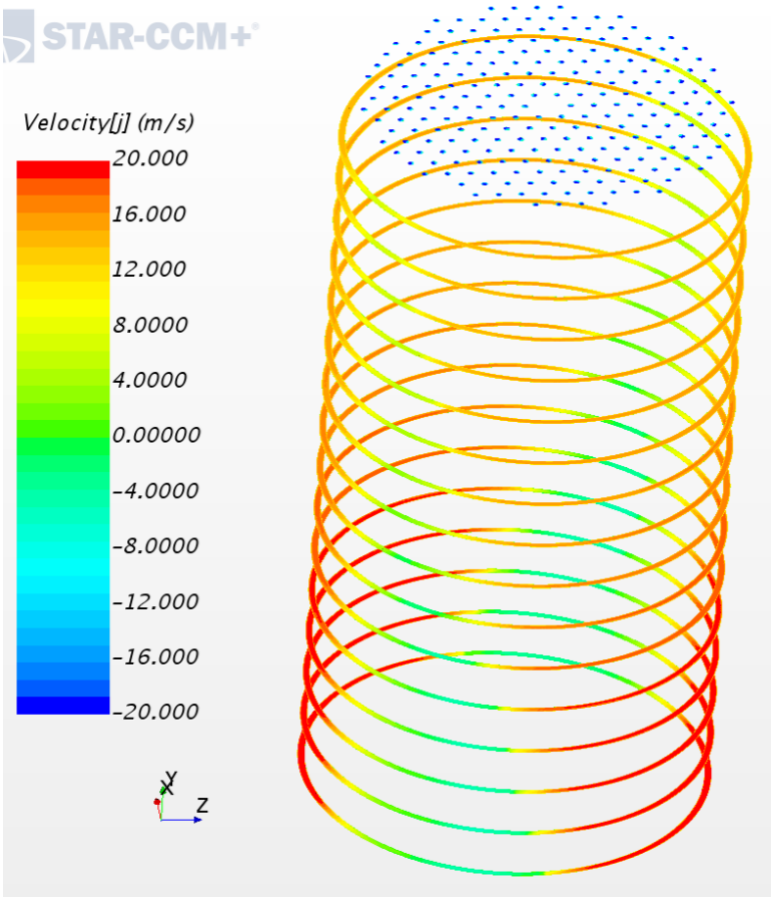

Figure 18. Vertical velocity contours in riser section of design modification 2 geometry.

Table III. Vertical velocity uniformity vs. vertical location within design modification 2 geometry.

Location	Uniformity, velocity *y* (%)	Average velocity *y* (m/s)	Standard deviation velocity *y* (m/s)
Riser section, inlet: *y* = 0.2 m	62.50875	12. 66932	10.59521
y = 0.3 m	66.00218	12.71071	9.715096
y = 0.4 m	68.87014	12.71446	9.017245
y = 0.5 m	70.94216	12.63583	8.506817
y = 0.6 m	73.21637	12.56183	7.945475
y = 0.7 m	76.43068	12.58666	7.140219
y = 0.8 m	79.99531	12.67211	6.151716
y = 0.9 m	82.63739	12.69717	5.362489
y = 1.0 m	84.62263	12.69698	4.778713
y = 1.1 m	86.49185	12.74261	4.228362
y = 1.2 m	87.93467	12.78183	3.789058
y = 1.3 m	88.93023	12.78796	3.480255
y = 1.4 m	89.62187	12.77648	3.255810
y = 1.5 m	90.14640	12.75525	3.087734
y = 1.6 m	90.60025	12.73747	2.950684
Riser section, outlet: *y* = 1.7 m	91.11820	12.75167	2.804701
Reflector channels: *y* = 1.8 m	87.20741	-16.29576	5.053888

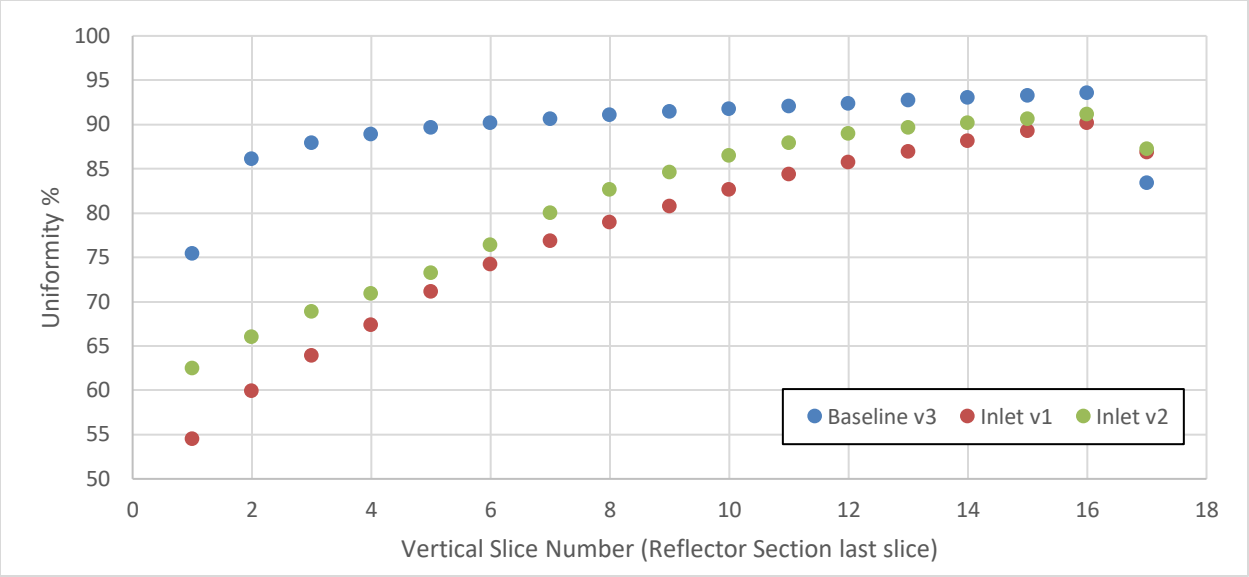

Figure 19. Uniformity of riser section vertical velocity.

With the newly elongated inlet ducts, the large eddies still dominate the flow within the top plenum, resulting in a near-tangential inlet angle at the top reflectors. However, the rotational flow about the shutdown rod increased. This spinning flow helped further reduce the pressure losses. Figure 20 and Figure 21 provide additional details.

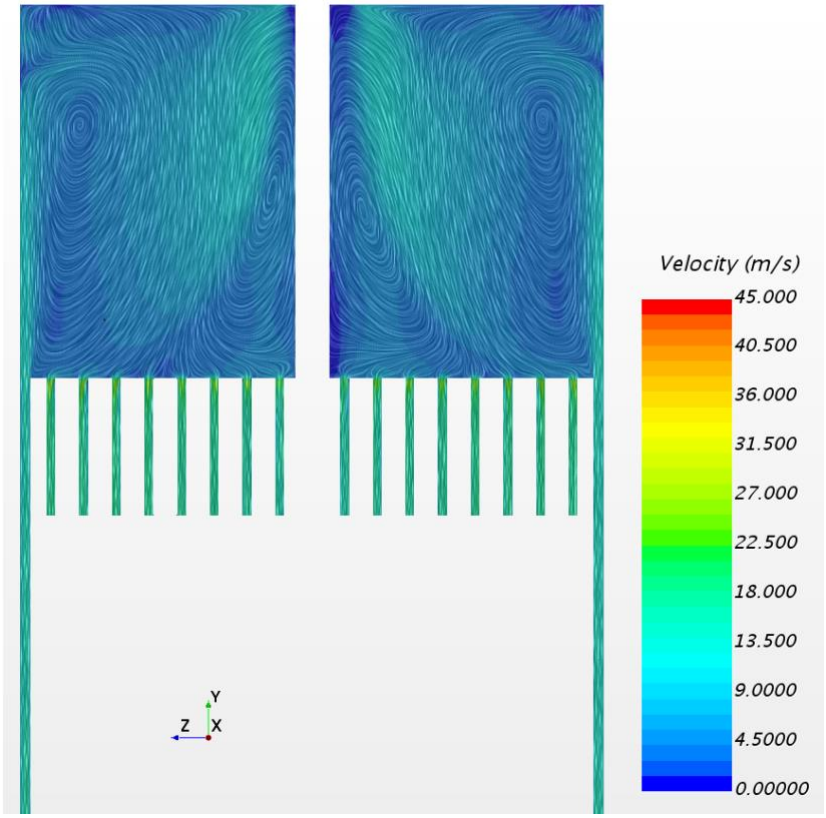

Figure 20. Coolant flow paths within the top plenum of design modification 2 geometry.

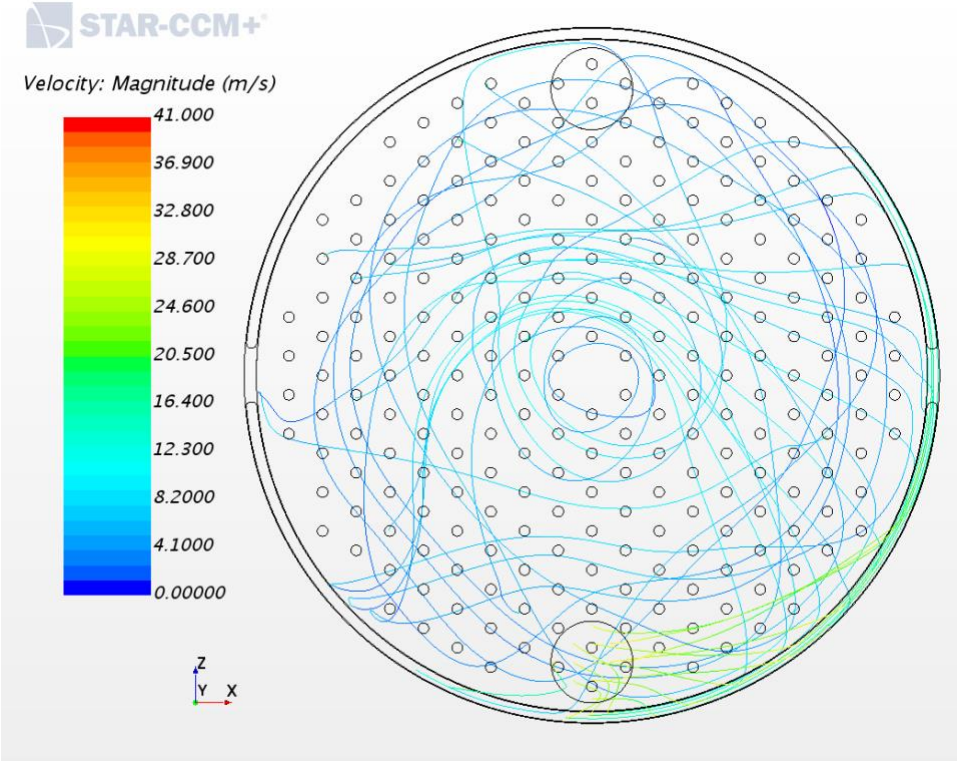

Figure 21. Streamlines of coolant flow paths within the top plenum of design modification 2 geometry.

Although the pressure drop caused by the inlet plenum was reduced further, the resulting effect within the riser section was minimal. Further designs were needed to address the vertical velocity uniformity while maintaining, or further reducing, the system pressure losses.

A-1.4 Inlet Plenum Design Modification 2b

To attempt to further direct the flow within the ducting geometry, internal turning veins were added to the design modification 2 geometry in hopes that the flow would spread within the ducting geometry. In turn, this would lead to a more uniform flow field within the riser section. Figure 22 and Figure 23 provide additional details.

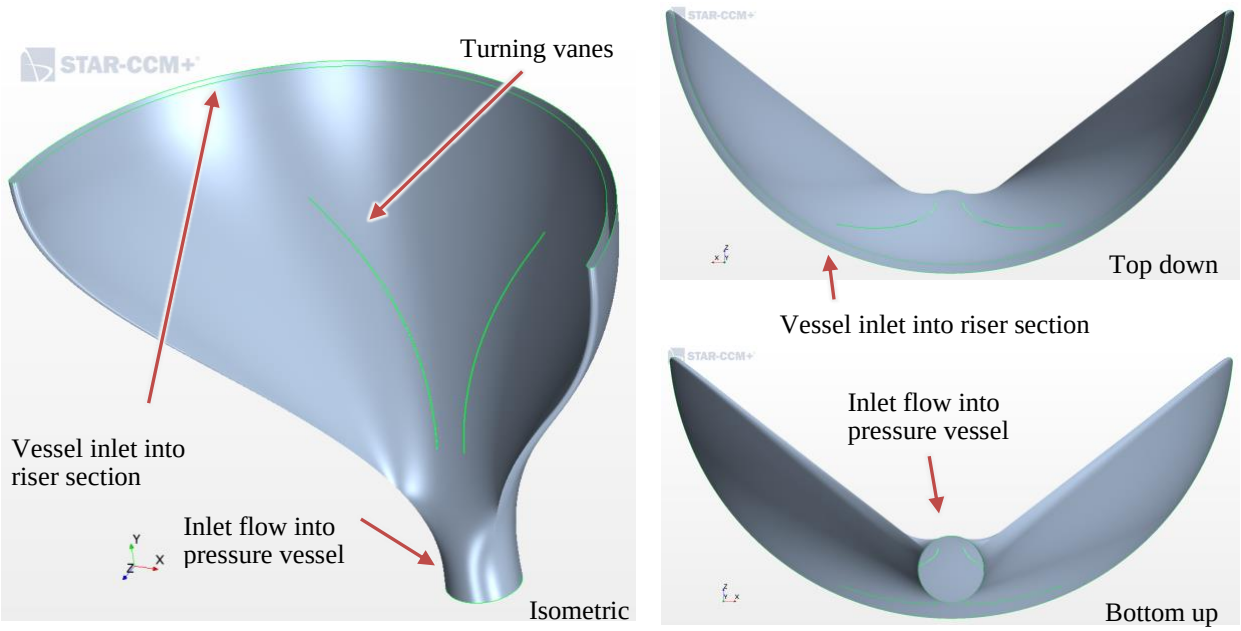

Figure 22. Various views of the design modification 2b inlet ducting geometry.

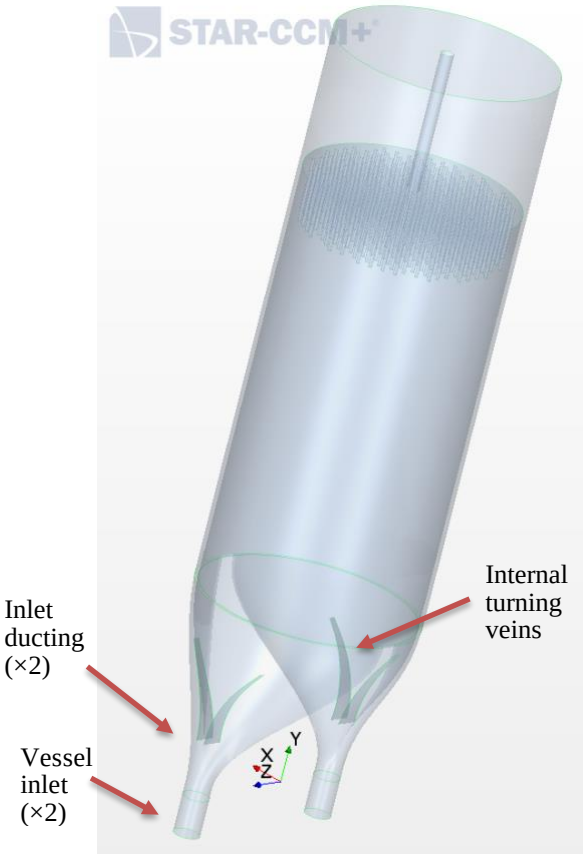

Figure 23. Inlet plenum design modification 2b geometry.

The overall pressure drop savings for the system remained stable at approximately 0.38 psid, which represents 26.9% of the total allowable limit for the entire system. Table IV provides additional details. The velocity uniformity within the riser section gained significant uniformity at the lower heights while losing some uniformity at the higher heights. This is a good trend, but more must be done to further spread the flow evenly within the inlet duct that leads to the riser section. Table V, Figure 24, and Figure 25 provide specific details.

Table IV. Breakdown of total pressure drop across design modification 2b geometry.

Location	P_{Total} (psi)	ΔP_T (psi)	System ΔP_T (psi) (outlet–inlet)
Inlet	1.015752E+03		
Riser section, inlet	1.015638E+03	-0.114	
Riser section, outlet	1.015557E+03	-0.081	
Outlet	1.015376E+03	-0.181	-0.376

Table V. Vertical velocity uniformity vs. vertical location within design modification 2b geometry.

Location	Uniformity, velocity *y* (%)	Average velocity *y* (m/s)	Standard deviation velocity *y* (m/s)
Riser section, inlet: *y* = 0.2 m	76.47408	12.67971	7.178798
y = 0.3 m	78.06692	12.68017	6.646704
y = 0.4 m	78.93700	12.67796	6.382370
y = 0.5 m	79.55937	12.67925	6.240981
y = 0.6 m	80.01535	12.65851	6.160226
y = 0.7 m	80.77185	12.67086	5.937589
y = 0.8 m	81.71310	12.69285	5.555963
y = 0.9 m	82.75993	12.70286	5.096351
y = 1.0 m	83.61519	12.68527	4.779637
y = 1.1 m	84.29140	12.65532	4.565789
y = 1.2 m	84.89433	12.61815	4.382736
y = 1.3 m	85.49228	12.57895	4.204373
y = 1.4 m	86.11887	12.55383	4.023373
y = 1.5 m	86.80289	12.54579	3.830684
y = 1.6 m	87.56915	12.55783	3.621602
Riser section, outlet: *y* = 1.7 m	88.43425	12.59883	3.395769
Reflector channels: *y* = 1.8 m	84.09532	-15.89895	5.988785

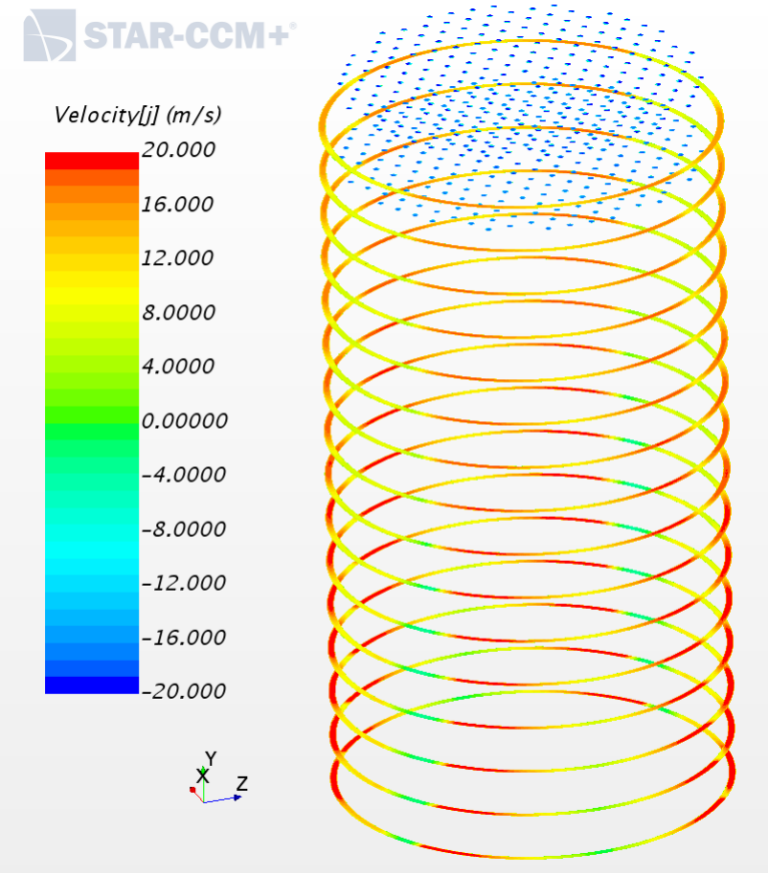

Figure 24. Vertical velocity contours in riser section of design modification 2b geometry.

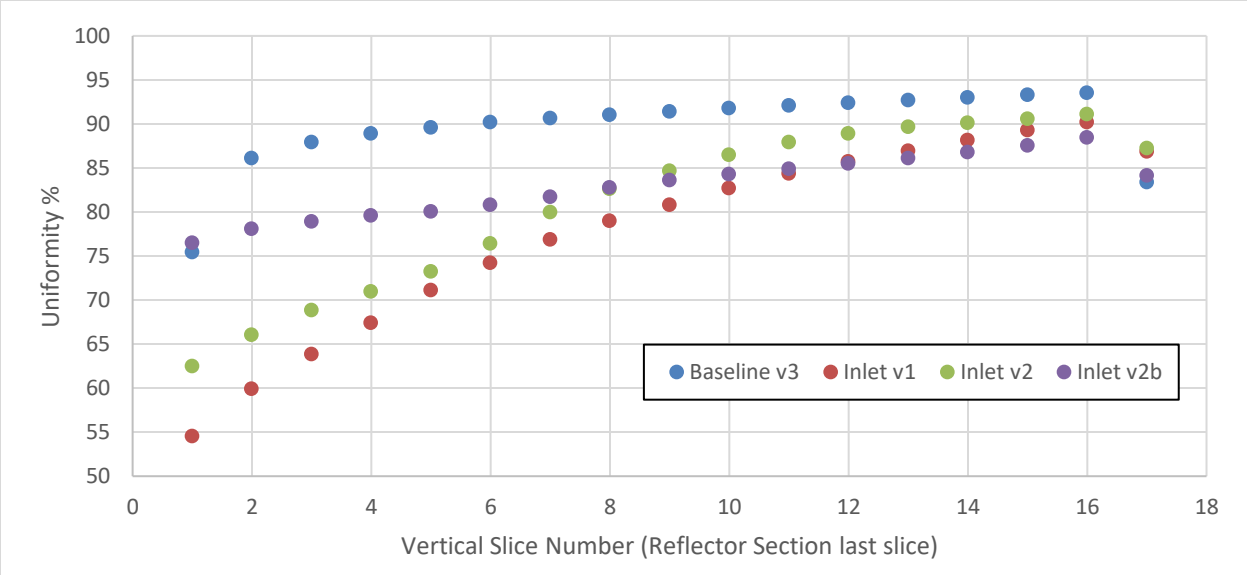

Figure 25. Uniformity of riser section vertical velocity.

The newly added turning veins within the inlet ducts did not significantly change the flow in the top plenum. The large eddies still dominate the flow within the top plenum with the rotational flow about the shutdown rod. Figure 26 and Figure 27 provide additional details. Adding the turning veins helped address the vertical velocity uniformity while maintaining, or further reducing, the system pressure losses. However, as shown in Figure 28, there are regions along the turning veins in which the internal flow is detaching and causing pockets of reversed flow. To continue increasing the vertical uniformity within the riser section, the issue of flow detachment must be addressed.

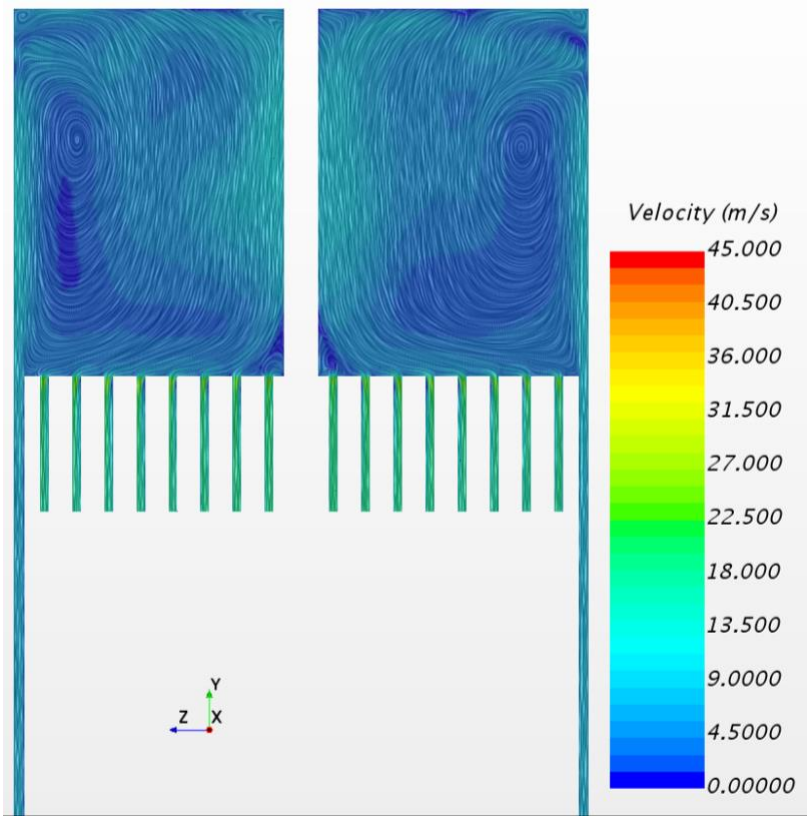

Figure 26. Coolant flow paths within the top plenum of design modification 2b geometry.

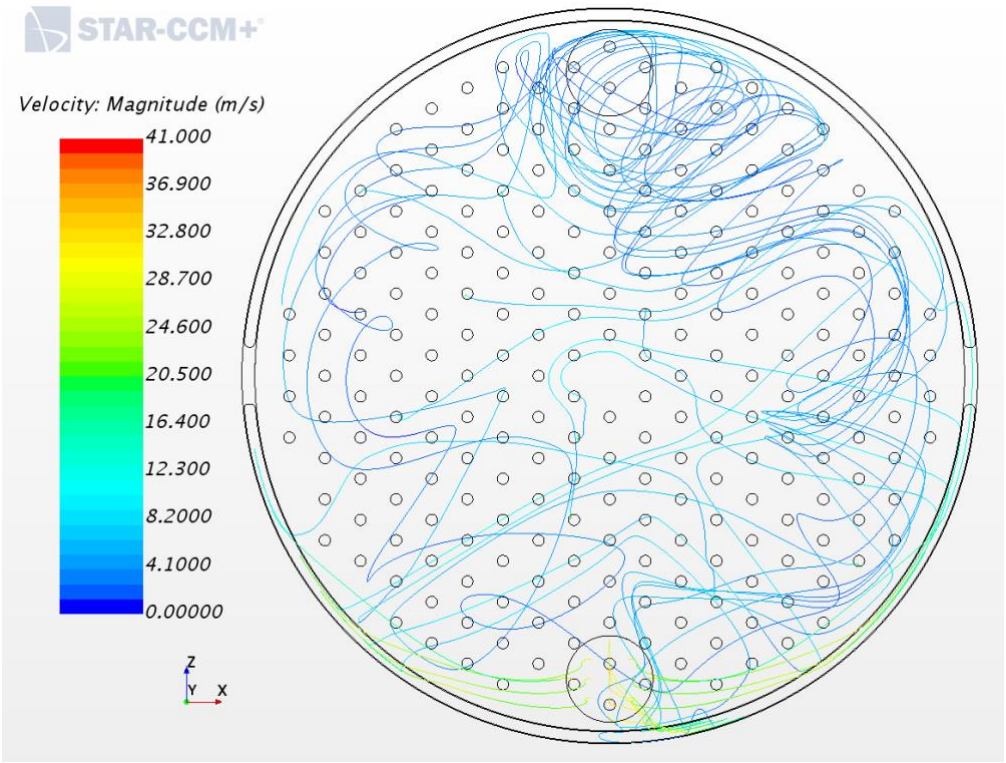

Figure 27. Streamlines of coolant flow paths within the top plenum of design modification 2b geometry.

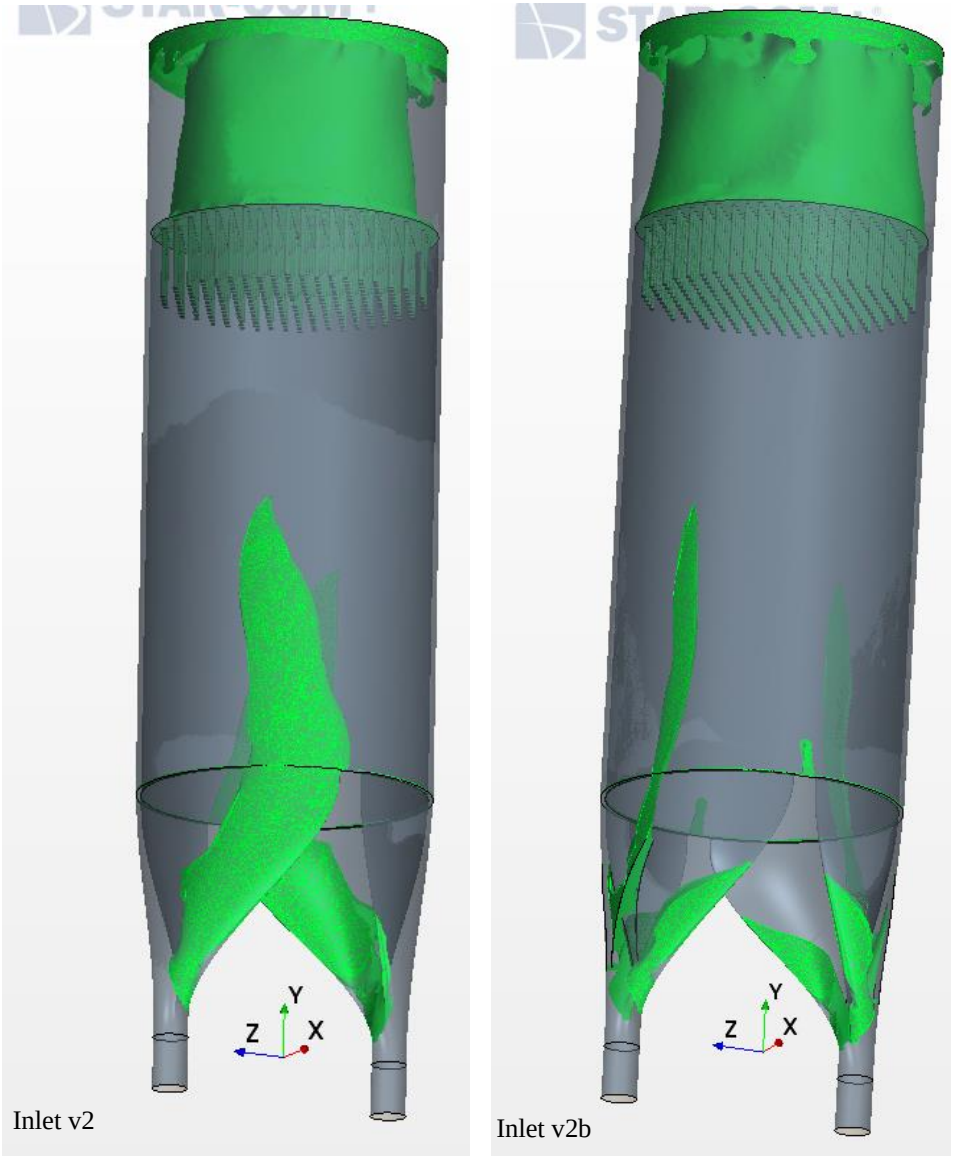

Figure 28. Isosurface of onset of reversed vertical flow (green).

A-1.5 Inlet Plenum Design Modification 2c

To attempt to remove the detachment of coolant flow on the turning veins, four slots were added along their lengths. This technique is borrowed directly from the aerospace community in which this method is used to introduce energized air back onto the top of the airfoils in an airplane split flap configuration. Here, it is intended to perform the same function: add energized coolant back onto the detached flow surface and remove the separated regions. The team hoped that adding these slots to the turning veins would make the flow continue to spread within the ducting geometry, leading to a more uniform flow field within the riser section. Figure 29 and Figure 30 provide additional details.

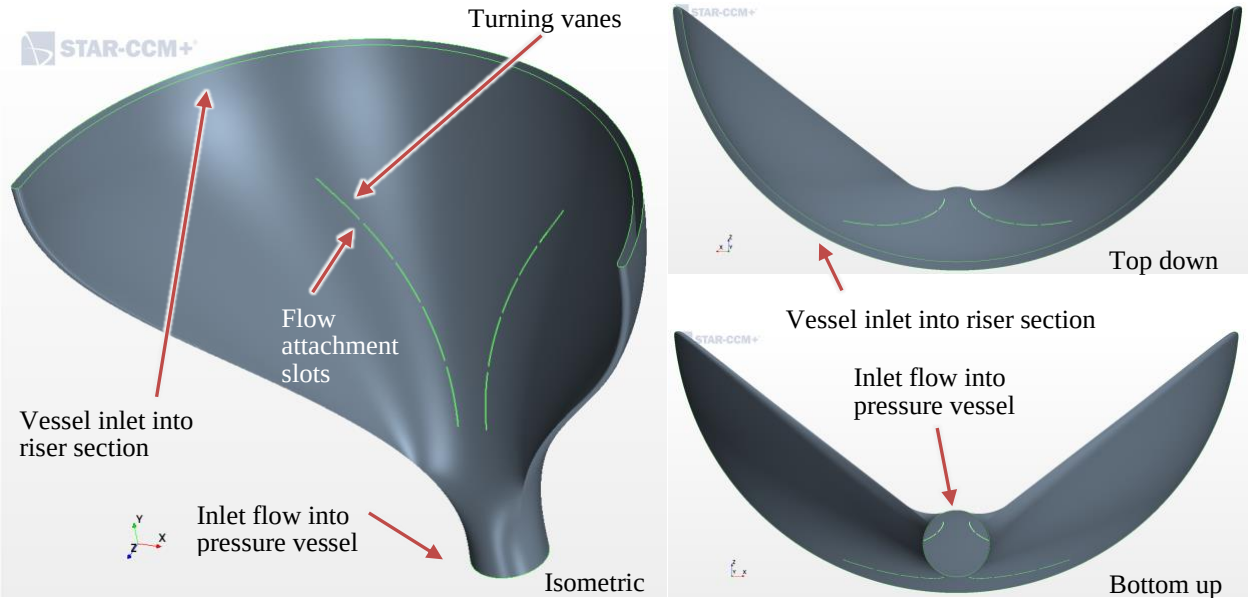

Figure 29. Various views of the design modification 2c inlet ducting geometry.

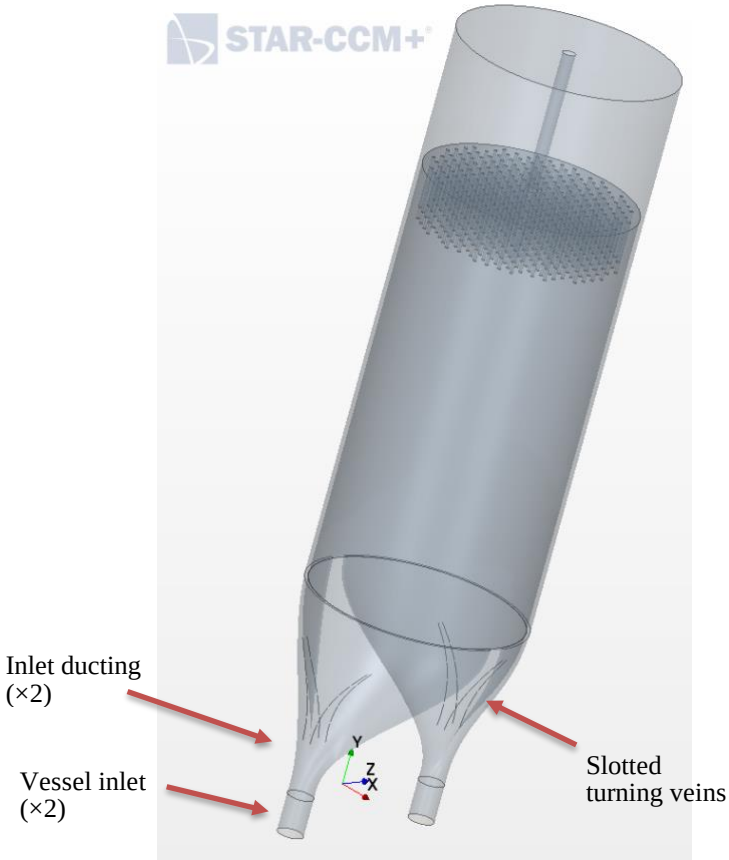

Figure 30. Inlet plenum design modification 2c geometry.

The overall pressure drop savings for the system remained stable at approximately 0.37 psid, which represents 26.2% of the total allowable limit for the entire system. Table VI provides additional details.

Table VI. Breakdown of total pressure drop across design modification 2c geometry.

Location	P_{Total} (psi)	ΔP_T (psi)	System ΔP_T (psi) (outlet–inlet)
Inlet	1.015743e+03		
Riser section, inlet	1.015630e+03	-0.113	
Riser section, outlet	1.015552e+03	-0.078	
Outlet	1.015376e+03	-0.176	-0.367

The velocity uniformity within the riser section remained mostly unchanged. Adding the slots to the turning veins did not lead to increased velocity uniformity within the riser section as desired. Table A-10, Figure 31, and Figure 32 provide specific details.

Table A-10. Vertical velocity uniformity vs. vertical location within design modification 2c geometry.

Location	Uniformity, velocity y (%)	Average velocity y (m/s)	Standard deviation velocity y (m/s)
Riser section, inlet: y = 0.2 m	75.92539	12.69368	7.144743
y = 0.3 m	78.17857	12.70297	6.338310
y = 0.4 m	79.79044	12.70923	5.818363
y = 0.5 m	81.03760	12.71138	5.479859
y = 0.6 m	82.05179	12.70717	5.233172
y = 0.7 m	82.93464	12.70280	5.021361
y = 0.8 m	83.75099	12.69878	4.816966
y = 0.9 m	84.54263	12.69078	4.607242
y = 1.0 m	85.32117	12.68442	4.393516
y = 1.1 m	86.07201	12.68677	4.182433
y = 1.2 m	86.79802	12.68995	3.975526
y = 1.3 m	87.48381	12.69090	3.776592
y = 1.4 m	88.13617	12.69891	3.588536
y = 1.5 m	88.74835	12.70976	3.413703
y = 1.6 m	89.33643	12.71761	3.246697
Riser section, outlet: y = 1.7 m	89.92377	12.72670	3.081545
Reflector channels: y = 1.8 m	83.58795	-15.87706	6.167667

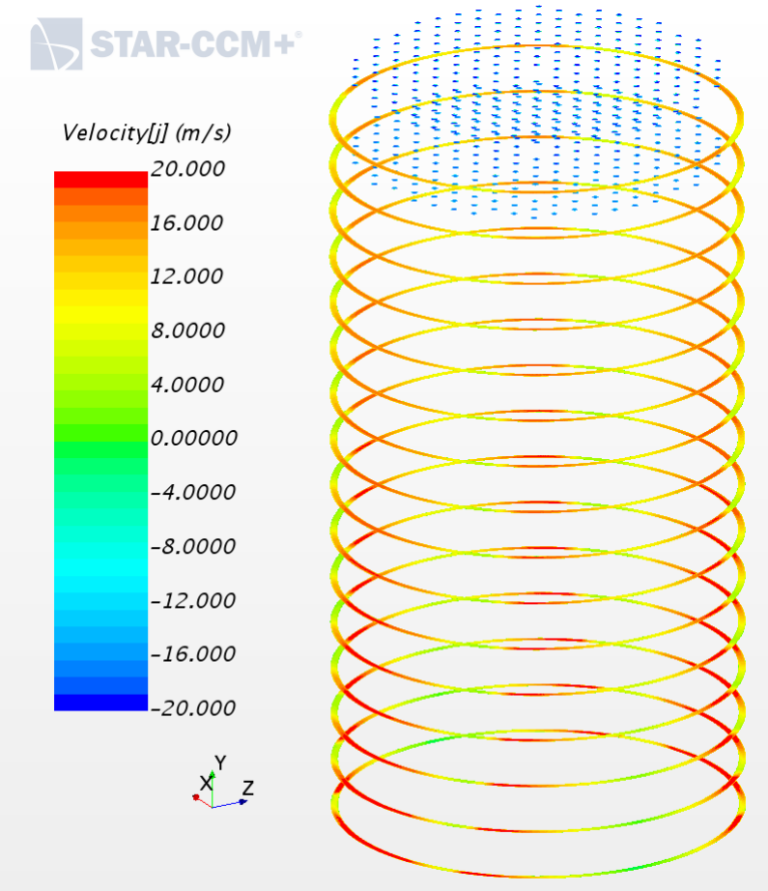

Figure 31**. Vertical velocity contours in riser section of design modification 2c geometry.**

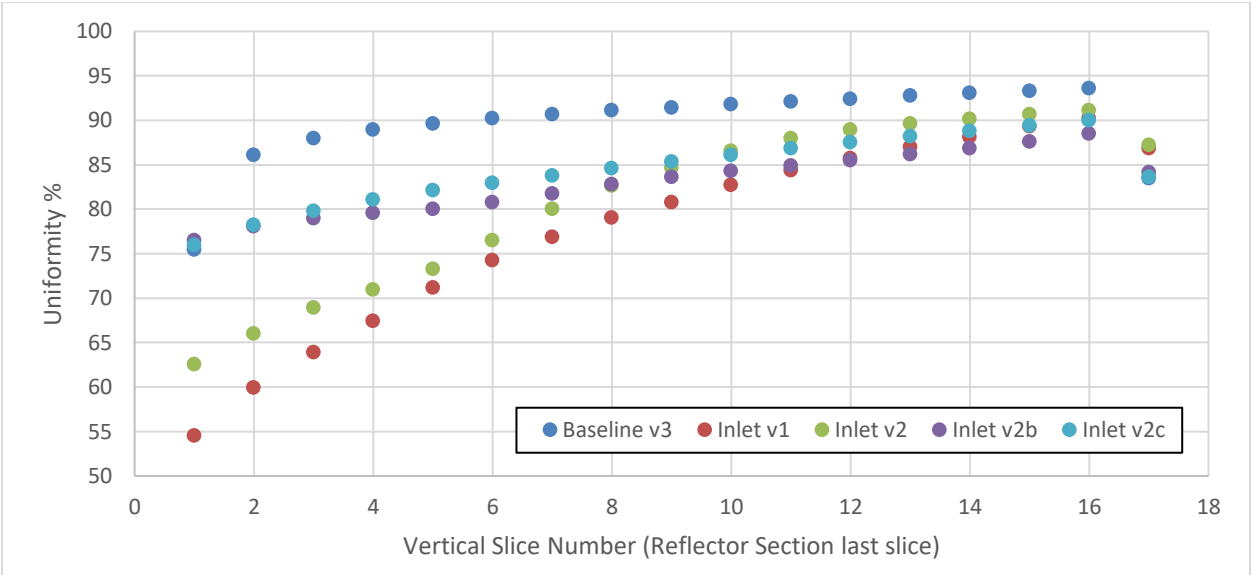

Figure 32. Uniformity of riser section vertical velocity.

The newly added slots within the turning veins did not significantly affect the large eddies within the top plenum. However, the rotational flow about the shutdown rod was eliminated. Figure 33 and Figure 34 provide additional details.

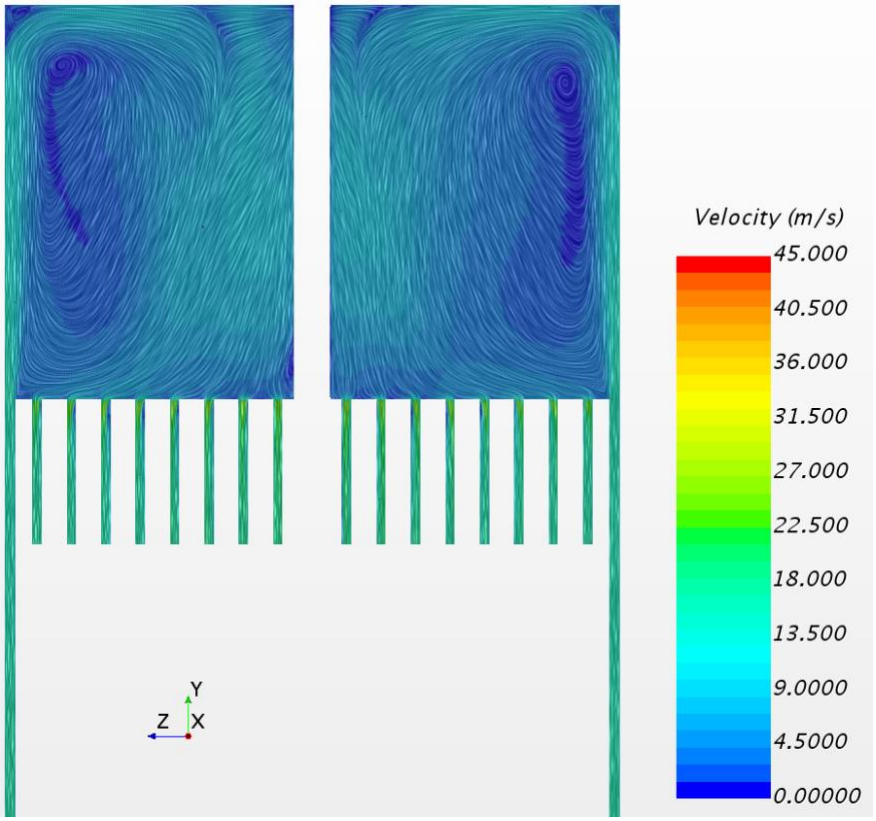

Figure 33. Coolant flow paths within the top plenum of design modification 2c geometry.

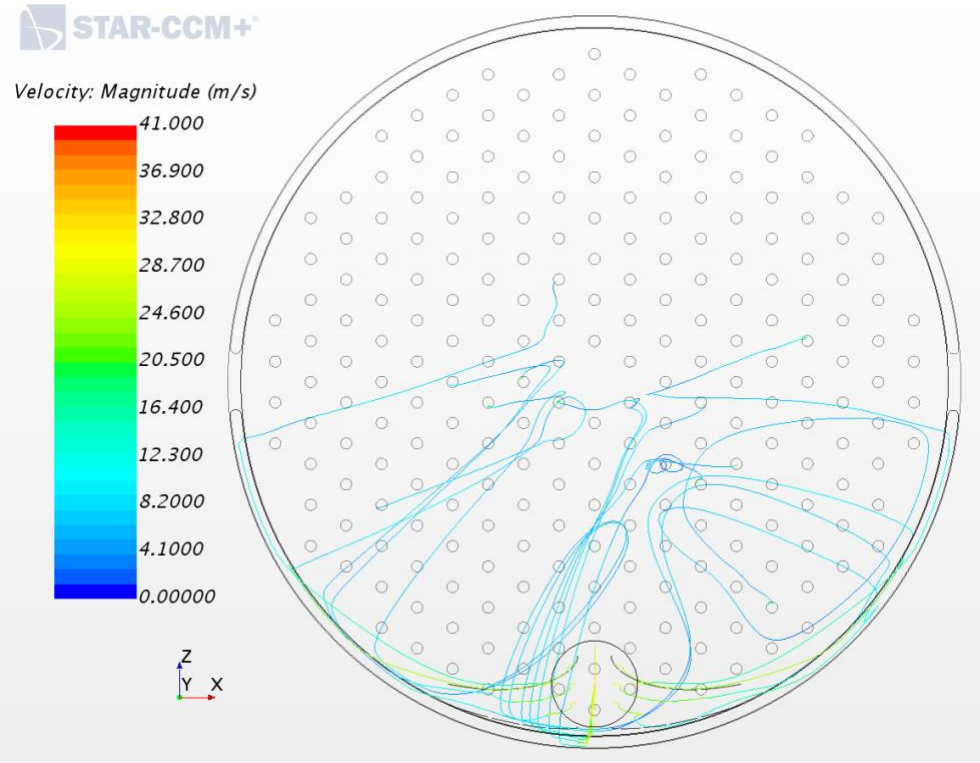

Figure 34. Streamlines of coolant flow paths within the top plenum of design modification 2c geometry.

Adding the slots within the turning veins helped address the internal attachment of the inlet ducts, as shown in Figure 35. However, the vertical velocity uniformity within the riser section still warrants further improvements, and a new approach will be needed to accomplish this.

Figure 35. Isosurface of onset of reversed vertical flow (green)

A-1.6 Inlet Plenum Design Modification 3

Although the design modification 2 series reduced the pressure drop significantly, it did not have the desired effect on the vertical velocity uniformity within the riser section. To attempt to increase uniformity, the inlet ducting was designed to create a rotating flow around the core barrel within the riser section. To accomplish this, the inlet tubes were pitched, and the corresponding inlets into the riser section were rotated one-fourth of the way around the pressure vessel. Figure 36 and Figure 37 provide additional details. The overall pressure drop savings for the system dropped even further to approximately 0.20 psid. This a savings of 74.7% over the baseline geometry and represents 14.3% of the total allowable limit for the entire system. Table VII provides additional details.

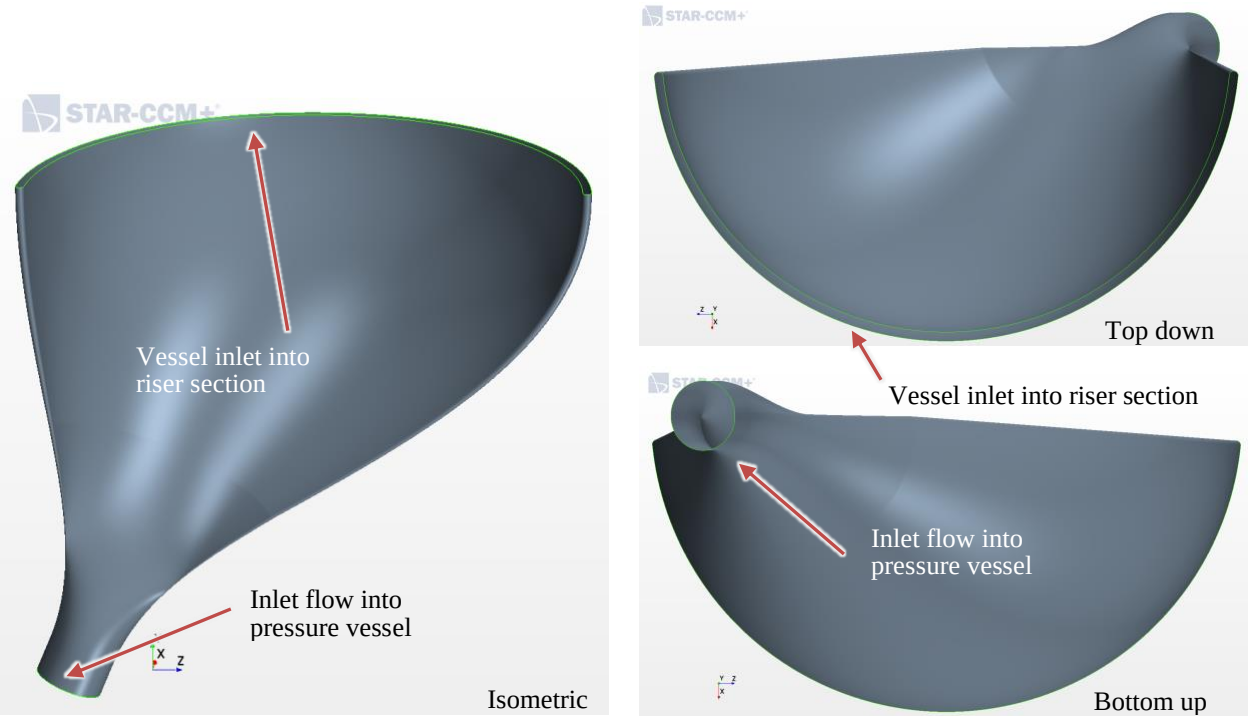

Figure 36. Various views of the design modification 3 inlet ducting geometry.

Figure 37. Inlet plenum design modification 3 geometry.

Table VII. Breakdown of total pressure drop across design modification 3 geometry.

Location	P_{Total} (psi)	ΔP_T (psi)	System ΔP_T (psi) (outlet–inlet)
Inlet	1.015517E+03		
Riser section, inlet	1.015459E+03	-0.058	
Riser section, outlet	1.015397E+03	-0.062	
Outlet	1.015315E+03	-0.082	-0.202

The velocity uniformity within the riser section increased to slightly better than baseline conditions. The rotating flow within the anulus riser section did an excellent job of elevating any potential for hot spots by unifying the fluid flow field. Table VIII, Figure 38, and Figure 39 provide specific details.

Table VIII. Vertical velocity uniformity vs. vertical location within design modification 3 geometry.

Location	Uniformity, velocity *y* (%)	Average velocity *y* (m/s)	Standard deviation velocity *y* (m/s)
Riser section, inlet: y = 0.2 m	84.61211	12.44830	4.764228
y = 0.3 m	86.92671	12.47981	4.195912
y = 0.4 m	88.40783	12.49311	3.740853
y = 0.5 m	89.59703	12.50662	3.293697
y = 0.6 m	90.55991	12.51895	2.949412
y = 0.7 m	91.33646	12.53818	2.702151
y = 0.8 m	91.97334	12.55901	2.516319
y = 0.9 m	92.49237	12.57775	2.372525
y = 1.0 m	92.9168	12.59665	2.258798
y = 1.1 m	93.26618	12.61726	2.167340
y = 1.2 m	93.55459	12.63496	2.029034
y = 1.3 m	93.79539	12.64598	2.029034
y = 1.4 m	93.98895	12.65767	1.978352
y = 1.5 m	94.14619	12.66600	1.936918
y = 1.6 m	94.27063	12.66812	1.904010
Riser section, outlet: y = 1.7 m	94.34573	12.67214	1.884077
Reflector channels: y = 1.8 m	84.01651	-9.484956	3.595186

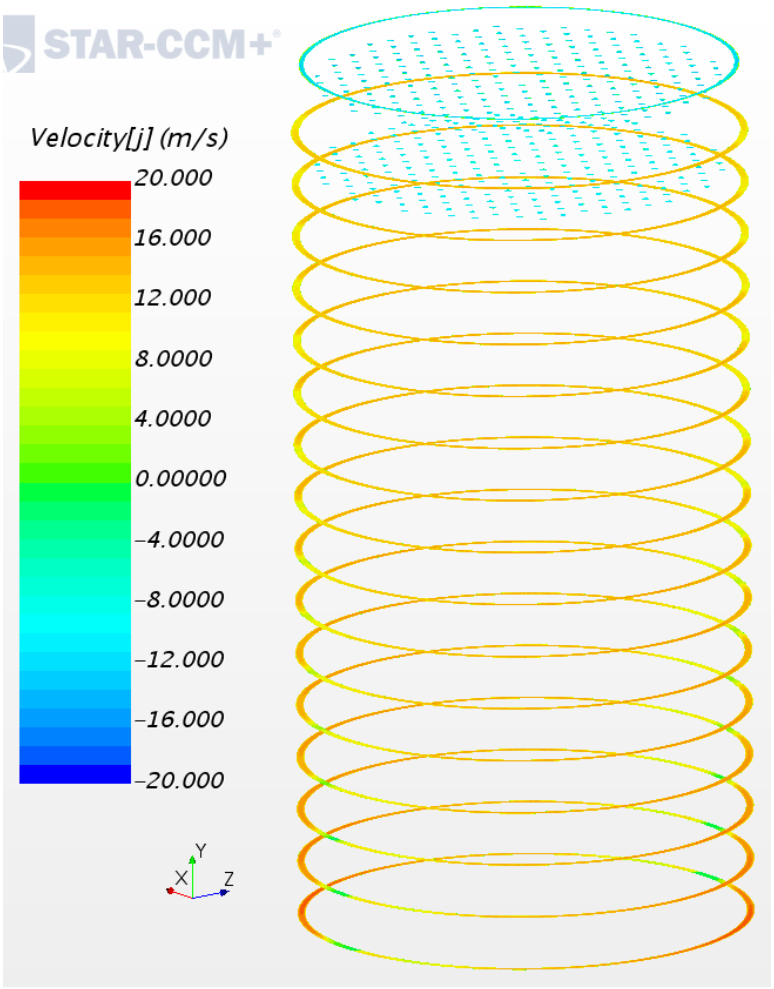

Figure 38. Vertical velocity contours in riser section of design modification 3 geometry.

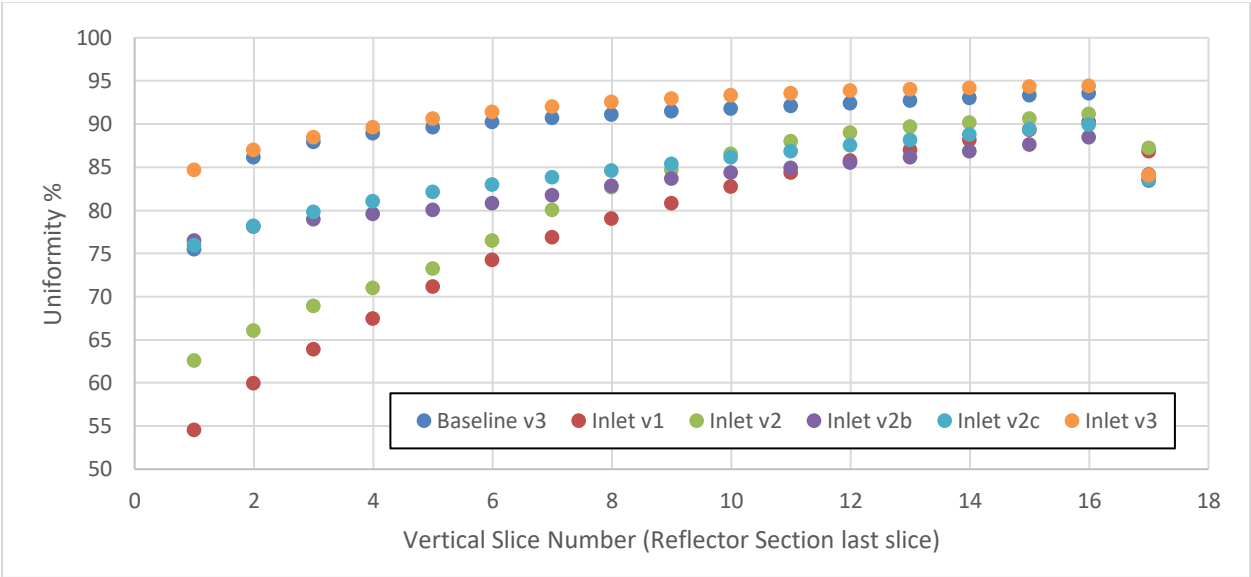

Figure 39. Uniformity of riser section vertical velocity.

With the rotating flow within the riser section, a large rotating flow within the top plenum is expected again. This is a desirable trait because the pressure drop within the top plenum reduced by almost half. Figure 40 and Figure 41 provide additional details.

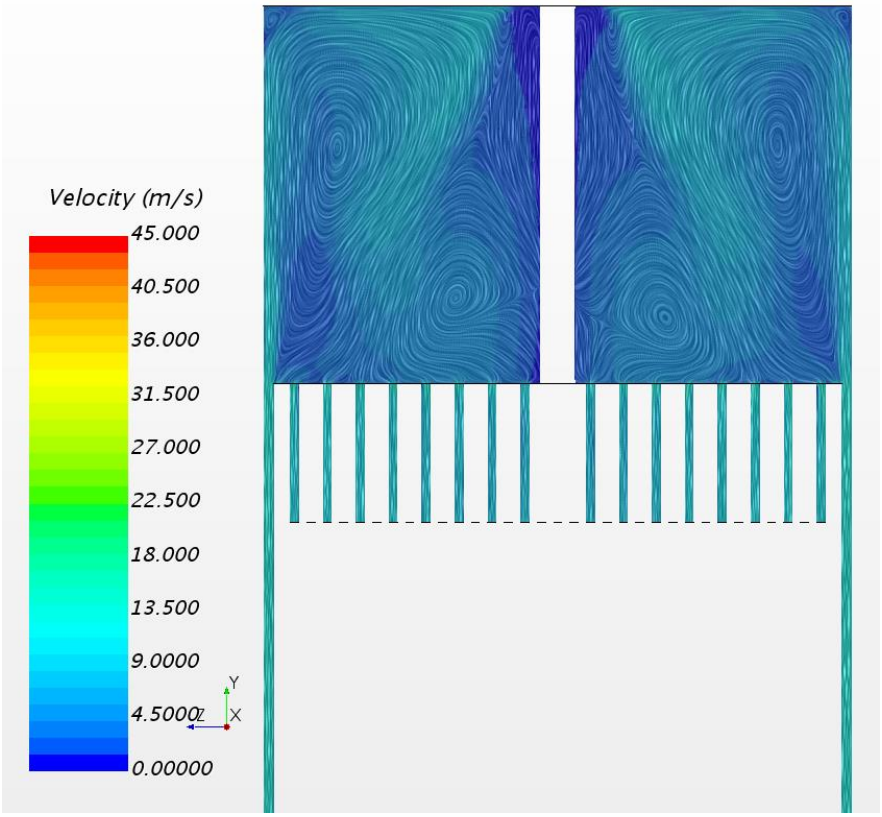

Figure 40. Coolant flow paths within the top plenum of design modification 3 geometry.

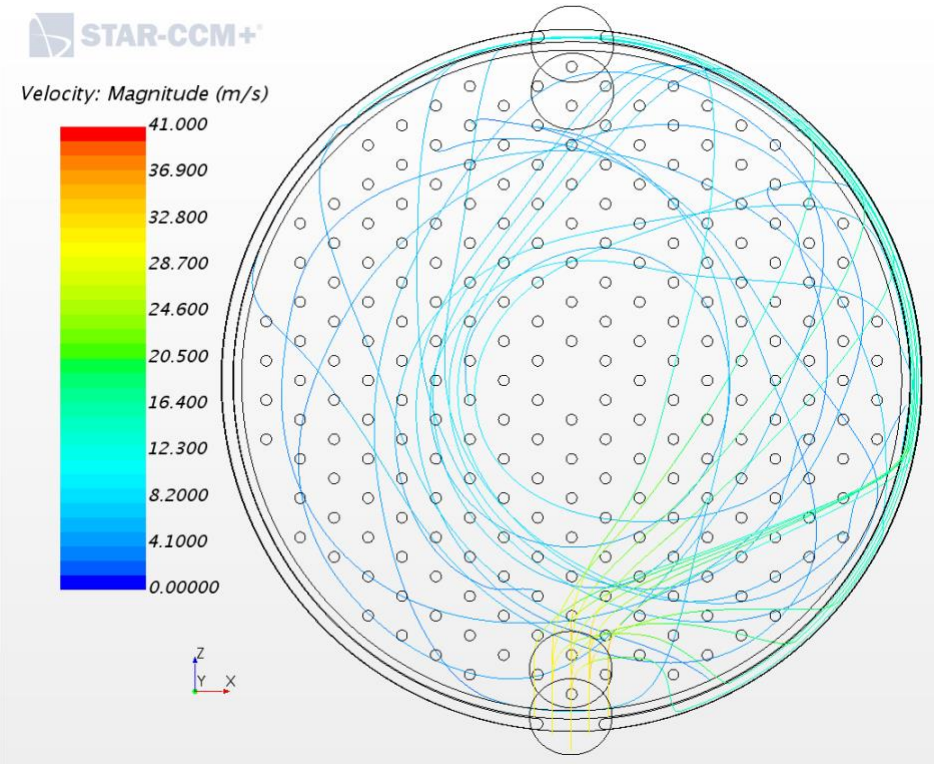

Figure 41. Streamlines of coolant flow paths within the top plenum of design modification 3 geometry.

A-1.7 Inlet Plenum Design Conclusions

System-level estimates for the allowable pressure loss across the pressure vessel and core were roughly one-tenth of an atmosphere, or 1.4 psid. However, initial baseline designs of the inlet plenum, riser section, and top plenums were evaluated at 0.8 psid, or 57.1% of the total pressure loss allowable. With the core and outlet plenums to yet be designed, further savings were needed. An inlet ducting that takes advantage of the flexibility of additive manufacturing was designed to rotate the flow, creating a uniform vertical velocity through the riser section and a rotating flow within the top plenum. This design reduced the pressure losses to 0.2 psid, or 14.4% of the total pressure loss allowable.